Advancing laser powder bed fusion with non-spherical powder: Powder-process-structure-property relationships through experimental and analytical studies of fatigue performance

Mohammadreza Asherloo [a], Madhavan Sampath Ramadurai [a], Mike Heim [b], Dave Nelson [b], Muktesh Paliwal [c], Iman Ghamarian [d], Anthony D. Rollett [e], Amir Mostafaei [a, *]

[a] Department of Mechanical, Materials and Aerospace Engineering, Illinois Institute of Technology, 10 W 32nd Street, Chicago, IL 60616, USA

[b] Nel Pretech Corporation, 8420 183rd Place, Tinley Park, IL 60487, USA

[c] Kymera International - Reading Alloys, Robesonia, PA 19551, USA

[d] School of Aerospace and Mechanical Engineering, University of Oklahoma, Norman, OK 73019, USA

[e] Department of Materials Science and Engineering, Carnegie Mellon University, Pittsburgh, PA, 15213, USA

* Corresponding author: A. Mostafaei (mostafaei@iit.edu)

Abstract

This study investigates the multifaceted interdependencies among powder characteristics (i.e., non-spherical morphology and particle size ranging 50-120 or 75-175 μm), laser powder bed fusion (L-PBF) process condition (i.e., contouring), post-process treatments (i.e., hot isostatic pressing (HIP) and mechanical grinding) on the pore, microstructure, surface finish, and fatigue behavior of additively manufactured Ti-6Al-4V samples. Microstructure analysis shows a phase transformation α′ → α+β microstructure after HIP treatment (at 899±14 °C for 2 h under the applied pressure of 1034±34 bar) of the as-built Ti-6Al-4V parts. The findings from pore analysis using micro-computed tomography (μ-CT) show an increase in sub-surface pores when relatively smaller powders are L-PBF processed including contouring. Surface optical profilometry reveals a decrease in surface roughness when fine powder is L-PBF including contouring. Pore analysis conducted through μ-CT reveals that the presence of lack-of-fusion pores within the L-PBF processed coarse powder is more pronounced when compared to the fine powder. Furthermore, HIP treatment does not eliminate these pores. The fracture failure in as-printed parts occurs at the surface, while the combination of HIP and mechanical grinding alters crack initiation to subsurface pore defects. Fractography reveals that HIP and as-built samples followed the facet formation and pseudo-brittle fracture mechanisms, respectively. Fatigue life assessments, supported by statistical analysis, indicate that mechanical grinding and HIP significantly enhanced fatigue resistance, approaching the benchmarks set by wrought Ti-6Al-4V alloy. A fatigue prediction model which considers the surface roughness as a micro-notch has been used.

Keywords: Additive Manufacturing; hydride-dehydride powder; Fatigue modeling; Micro-computed tomography; Surface roughness; Statistical analysis.

1. Introduction

Two common types of Ti-6Al-4V powder being used in the fusion-based additive manufacturing (AM) processes are made by gas atomization (GA) or plasma rotating electrode process (PREP) with a resultant spherical particle morphology [1]. Typically, spherical powder show high packing density and high flowability [2], both of which are critical aspects in powder bed AM. However, there are two main drawbacks including trapped gas bubbles within powder particles (mainly GA) [3] and the high cost of powder production (which is much higher in PREP powder compared to GA powder) [4,5]. As a result, alternative powder production methods are increasingly appealing to powder producers, researchers, and AM machine manufacturers, especially if these methods can lower costs, reduce emissions, increase the availability of metal AM feedstock, and promote sustainability. Mechanical techniques, for instance, enable the reuse of scrap materials; the U.S. Army has shown interest in using retired weapon systems and military vehicles as feedstock for AM processes, thereby reducing logistical burdens for on-demand, on-site manufacturing [6,7].

Regarding titanium alloys, hydride-dehydride (HDH) process results in a low-cost powder with controlled chemistry and no entrapped gas pore inside the powder particles, although, the final powder shape is non-spherical. The non-spherical nature of the HDH powders would affect powder packing density, powder flow, laser-matter interaction and melt pool dynamics during L-PBF AM. In an attempt to L-PBF process the non-spherical Ti-6A-4V powder, Asherloo *et al.* [8] and Wu *et al.* [9] showed that the packing density of non-spherical powder with particle size ranging between 50-120 µm (based on the manufacturer's powder cut using a sieve) was ~55 %, only ~3 % less than the GA powder (~58 %), while parts with a relative density of > 99.9 % were manufactured. To show the printability of non-spherical HDH powder in the electron beam powder bed fusion (EB-PBF) process, Narra *et al.* [10] implemented the process map optimization and reported that parts with relative density of > 99.9 % were fabricable. Guzman *et al.* [4] also developed of a process map to optimize the L-PBF process for the use of non-spherical Ti-53%Nb powder and were able to manufacture parts with a relative density of > 99.9 %. Yang *et al.* [11] investigated the mixing of spherical CP-Ti powder with HDH CP-Ti powder with different ratios and showed that the relative density of > 98 % was achievable through L-PBF. Cunningham *et al.* [3] used GA and PREP powders to manufacture L-PBF Ti-6Al-4V parts. Through computed tomography, they found a higher fraction of pores—both lack of fusion and keyhole pores—in parts produced using GA powder compared to the PREP powder. This was attributed to a higher fraction of trapped gas pores within the powder and lower packing density. After hot isostatic pressing (HIP), the pores were eliminated, resulting in a reported density of 99.99 % for both powder types. It is worth noting that the authors did not investigate a bulk sample including the sub-surface defect region in their computed tomography analysis, leaving open the question of how HIP would affect the elimination of sub-surface pores in specimens printed with spherical powder. Studies on use of non-spherical powder in L-PBF highlight the printability of non-

spherical HDH powder regardless of the composition of the alloy or the AM process, however, here the first knowledge gap arises regarding the effect of powder size distribution on the final properties (e.g., surface finish and fatigue performance) of the parts.

Compared to machined wrought Ti-6Al-4V alloys, as-built L-PBF processed parts usually show lower fatigue endurance associated with surface roughness, textured microstructure, high residual stress, and pore content [12]. Yang *et al.* [13] investigated the effect of heat treatment on the fatigue performance of L-PBF processed Ti-6Al-4V parts and reported that heat treatment at 850 °C increased fatigue life drastically from 3.55×10^4 cycles to 3.59×10^6 cycles under 500 MPa uniaxial loading, which was attributed to the microstructure refinement and reduction of residual stress after heat treatment. Moon *et al.* [14] studied the effect of surface roughness and internal pore on the fatigue life of L-PBF processed Ti-6Al-4V parts using neural networks and reported that the surface roughness had higher impact on the fatigue life compared to the pore content. Moreover, after removing the surface roughness, the fatigue life was highly dependent on the pores of the parts, specifically, the pores that were exposed to the surface. Asherloo *et al.* [15] used non-spherical Ti-6Al-4V powder to L-PBF process fatigue samples and tested them under as-built and mechanically ground conditions. They showed that in the as-built condition, the high surface roughness act as crack initiation sites and in the mechanically ground condition, when the stress is high, the pores exposed to the surface acted as the crack initiation cotes, while at the low stress levels, the sub-surface pores played a key role in the crack nucleation. These studies covered the impact of various parameters on the fatigue life of the L-PBF processed Ti-6Al-4V parts, however, all the parameters have been individually investigated. Thus, the second knowledge gap is the effect of combination of these parameters (i.e., powder characteristics, pore content, post-process treatments, and surface roughness) on the fatigue performance of the L-PBF process Ti-6Al-4V parts.

The decrease in remaining pore is highly significant because pores within the sample can serve as potent stress concentrators, potentially causing failure, particularly when subjected to fatigue loading. The effect of post-process treatments on the fatigue properties of the L-PBF processed Ti-6Al-4V parts has been extensively investigated. Benedetti *et al.* [16] studied the effect of HIP at 920 °C under 100 MPa for 2 h on the fatigue performance of L-PBF processed Ti-6Al-4V parts and reported that HIP process did not change the fatigue performance due to the fact that HIP does not change the surface roughness of the parts and micro-notches on the surface decrease the fatigue life. Roudnicka *et al*. [17] drew the same conclusion regarding the effect of HIP on the fatigue performance of the L-PBF processed Ti-6Al-4V parts and stated that the effect of HIP is negligible when the surface condition is in the as-built state. Leuders *et al*. [18] combined the HIP and surface machining on the fatigue life of the L-PBF processed Ti-6Al-4V parts and showed that the fatigue limit increased from 2.7×10^4 to 10^6 cycles after machining. Moreover, Kasperovich *et al*. [19] studied the effect of machining on the fatigue performance of the L-PBF processed Ti-6Al-4V parts and were able to increase the fatigue limit of the parts from 5.6×10^3 cycles to 2×10^4 cycles.

They also tested samples after HIP + machining process and reported the increase in fatigue life up to 10^7 cycles. Recently, Alegre *et al*. [20] investigated HIP treatment at 850 °C and applied pressure of 200 MPa on the fatigue performance of L-PBF processed Ti-6Al-4V parts and reported that the combination of HIP and machining improved the fatigue performance such that it was comparable to the fatigue performance of the wrought samples. These studies show that the HIP process alone does not significantly impact the fatigue life of the parts. However, when combined with machining to remove surface roughness and sub-surface pore defects, fatigue performance improves. It is important to note that the HIP process addresses microstructure-driven fatigue behavior, while machining targets surface-defect-driven fatigue behavior.

The current study will cover knowledge gaps of the impact of (i) powder characteristics including particle size distribution, (ii) contouring during L-PBF process, and (iii) post-process treatments such as HIP treatment and surface griding on the fatigue life of L-PBF processed non-spherical Ti-6Al-4V powder. The AM presents a unique challenge, as assessing material properties alone may not fully represent the performance of real-world components. Machining AM parts often exclude the advantages of AM. However, the current work explores various surface conditions and porosity to investigate the effects of defect-population on fatigue performance. This is particularly important when the as-built surface condition is considered for applications such as bioimplants where surface roughness is a desirable feature as opposed to a defect. In-depth microstructure observations and texture analysis using scanning electron microscopy and μ-CT, surface roughness analysis through optical profilometry and μ-CT, and uniaxial fatigue life under different specimen conditions (i.e., pore content and surface finish) will leverage our understanding of correlating powder-process-structure-property relationships in L-PBF processed Ti-6Al-4V parts. The optimal combination of post-process treatments is presented to achieve a fatigue performance close to that of the wrought Ti-6Al-4V samples.

2. Experimental procedures

2.1 Laser powder bed fusion process

Two batches of HDH Ti-6Al-4V powder (Kymera International – Reading Alloys) with non-spherical powder morphology (shown in Figure 1) and particle size distributions (PSD) of 50-125 μm (fine) and 75-175 μm (coarse) were used. These PSD values are from the manufacturer based on their sieve sizes used to select the powder. The powder chemistry is given in Table 1. Morphology and size distribution of the used powders are shown in Figure 1.

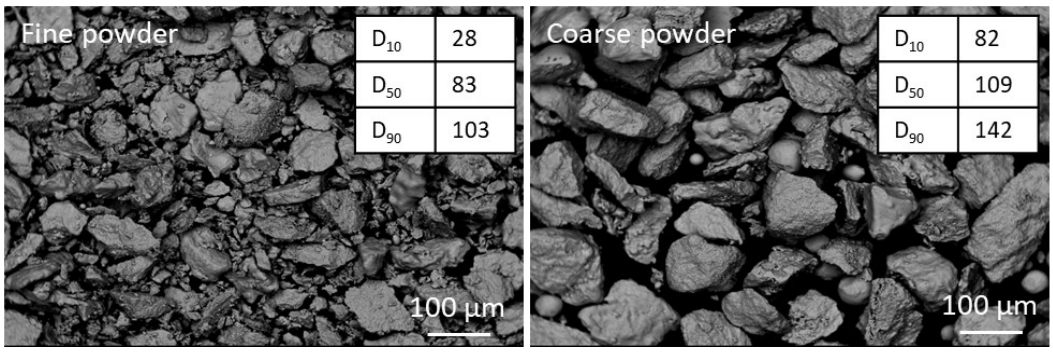

Figure 1. Scanning electron microscope images of the used fine and coarse non-spherical Ti-6Al-4V powder.

Table 1. Powder chemistry for the nominal Ti-6Al-4V and the HDH powder provided by the manufacturer [wt.%]. The HDH powder chemistry is equivalent to the grade 5 Ti-6Al-4V.

	Ti	Al	V	Fe	C	H	N	O
ASTM B 348 [21]	Bal.	5.5-6.75	3.5-4.5	< 0.40	< 0.08	< 0.015	< 0.05	< 0.20
Fine powder	Bal.	6.08	3.88	0.19	0.02	0.005	0.02	0.17
Coarse powder	Bal.	6.02	3.92	0.22	0.03	0.006	0.02	0.17

Dimensions of the designed fatigue samples was illustrated in Figure 2A. A total 85 fatigue samples were made according to the build layout shown in Figure 2B,C for both fine and coarse powders. The optimum L-PBF process parameters were selected based on our earlier studies in [8,22,23]: laser power of 370 W, laser scan speed of 1250 mm/s, hatch spacing of 90 µm, layer thickness of 60 µm, scan rotation of 67°, parallel stripes scan strategy, and contours including contour 1: 190 W, 1200 mm/s, and 300 µm inward offset and contour 2: 190 W, 1200 mm/s, and no inward offset. Contouring refers to a scanning strategy used during the printing process to refine the surface quality and dimensional accuracy of a part. Specifically, it involves an additional laser scan along the outer edges (contours) of a part after the main infill or bulk region has been processed. The contour scan is performed with adjusted laser parameters, typically with lower power and slower scan speed compared to the bulk scanning. To study the role of contour on surface roughness, above mentioned contouring is labeled as contour printing (56 specimens) and some other samples (29 specimens) were made without using contouring. After the L-PBF process, a stress-relief treatment was performed at 650 °C for 2 h under an argon atmosphere, which also facilitated the $\alpha' \rightarrow \alpha + \beta$ transformation [24].

Half of the L-PBF processed samples (with or without contouring) were HIPed at 899±14 °C for 2 h under the applied pressure of 1034±34 bar. Also, the gauge section of samples (selected ones to test effect of surface roughness reduction after grinding) was mechanically ground with sandpapers up to 1200 grit to remove the surface roughness. A summary of the labeled samples under specific conditions are provided in

Table 2.

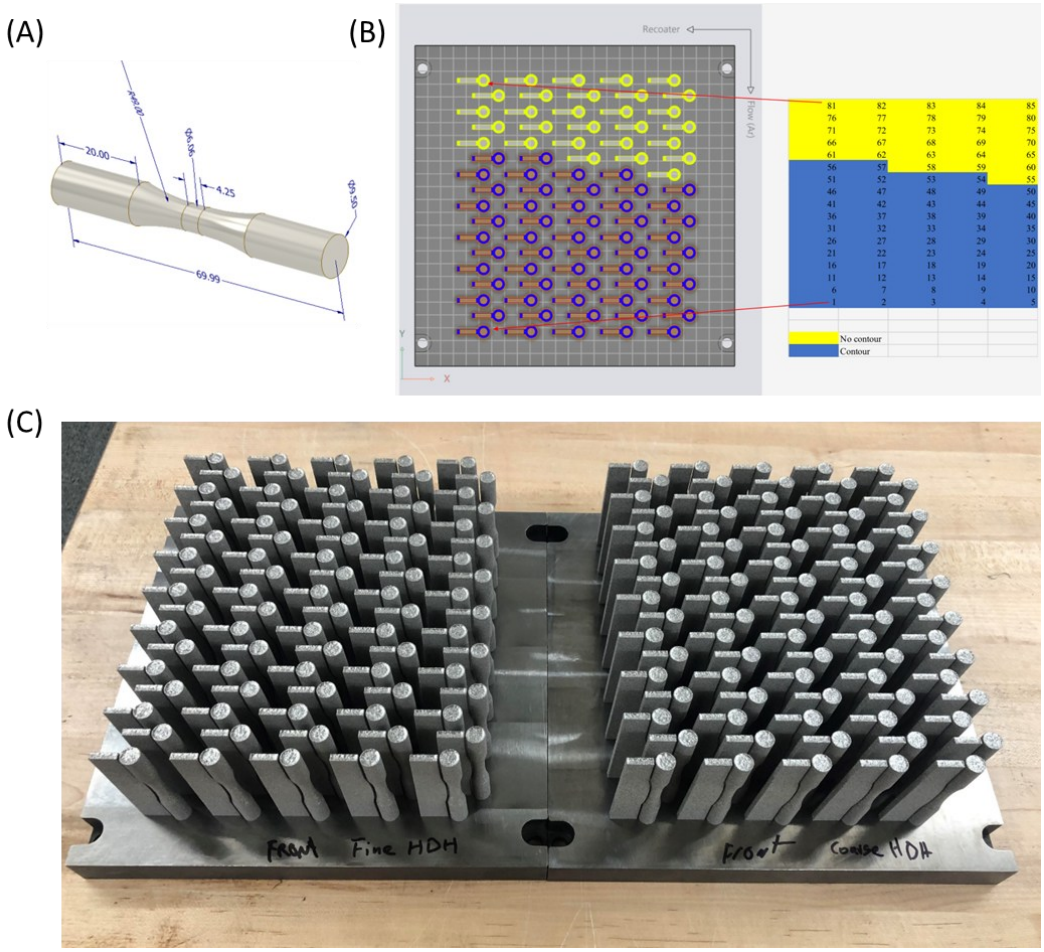

Figure 2. (A) Designed fatigue specimen indicating dimensions in mm. (B,C) Build layout showing the total number of 85 samples were made using fine and coarse powder for fatigue testing.

Table 2. An overview of all the samples' conditions including the powder size, heat treatment, surface treatment, and contouring.

Samples	Powder type	HIP treatment	Surface condition	Contouring
AB-C-C	Coarse	No	As-built	Yes
AB-C-NC	Coarse	No	As-built	No
AB-F-C	Fine	No	As-built	Yes
AB-F-NC	Fine	No	As-built	No
HIP-C-C	Coarse	Yes	As-built	Yes
HIP-C-NC	Coarse	Yes	As-built	No
HIP-F-C	Fine	Yes	As-built	Yes
HIP-F-NC	Fine	Yes	As-built	No
AB-C-G	Coarse	No	Mechanically Ground	Removed by grinding
AB-F-G	Fine	No	Mechanically Ground	Removed by grinding
HIP-C-G	Coarse	Yes	Mechanically Ground	Removed by grinding

HIP-F-G	Fine	Yes	Mechanically Ground	Removed by grinding

AB: As-built, HIP: Hot isostatically pressed, F: Fine, C: Coarse, C: Contour, NC: Non-contour, G: Ground

2.2 Characterizations

The microstructure and texture of the as-built and HIP treated parts were characterized after metallographic preparation using sandpapers up to 1200 grit size followed by polishing using a series of suspensions including 3 μm, 1 μm, and 0.05 μm alumina solutions and 0.04 μm colloidal silica solution. The etchant used in this study was Kroll's reagent (92 ml of distilled water, 6 ml of nitric acid, and 2 ml of hydrofluoric acid).

Microstructures were observed using a digital optical microscopy (model Keyence VHX 7100), field emission scanning electron microscope (FE-SEM, model JEOL JSM-6701 F), electron backscatter diffraction (EBSD, Oxford detector installed on JEOL 5900LV SEM). For the EBSD analysis, the acceleration voltage and step size were set at 20 keV and 0.3 μm, respectively. The AzTec software was used to collect EBSD data, then HKL Channel 5 software along with analysis using MTEX package were used to post-process and analyze data [25]. Surface roughness was collected using Keyence optical microscope from the gauge section on eight different sides.

To quantify pore and surface roughness, micro-computed tomography (μ-CT) was used to collect data from the gauge section of the fatigue specimens using a Zeiss Merotom 899 under 85 kV and 47 mA and final spatial resolution of 7 μm/pixel. Post-process and visualization of the μ-CT data was carried out using the VGSTUDIO software. To analyze pore size, the pore volume was assumed to correspond to a spherical shape, and the radius was then calculated for each pore. The quantification of pore sphericity in VGSTUDIO involves calculating the volume of pore and surface area from 3D scan data, determining the equivalent sphere's surface area, and then using the sphericity formula to assess how spherical the pore is.

An MTS 880 mechanical testing machine was used to perform fatigue tests. A uniaxial cyclic loading of fully reversed tension-compression ($R = -1$) experiment was carried out in air under frequency of 30 Hz. Microscopy observations including optical and SEM were conducted to study fracture surfaces. Three specimens were tested under each condition.

X-ray diffraction pattern analysis (XRD) involved using a Thermo ARL X-ray diffractometer with Cu-Kα radiation ($\lambda = 1.5406$ Å, 35 kV, and 30 mA). The gauge areas were tested in both as-built and mechanically ground conditions to assess residual stress. The analysis spanned a 2θ range from 30-100º, with a scan speed of 1 s per step and a step size of 0.02º, all conducted at room temperature. The identification of potential phases and determination of crystallographic parameters relied on the Powder Diffraction File database [26]. Rietveld refinement procedures were performed using the MAUD software [27].

2.3 . Statistical analysis

To elucidate the complex interrelationships among the various process parameters influencing the fatigue performance of Ti-6Al-4V specimens manufactured by L-PBF, we employ multiple statistical correlation tests in our study. These tests—including Pearson's correlation coefficient, Spearman's rank correlation, and ANOVA with Tukey post-hoc analysis—are applied to quantify the strength and significance of associations between factors such as powder characteristics, laser contouring conditions, post-process hot isostatic pressing, mechanical grinding, and the resulting mechanical properties. By using these statistical methods, we aim to uncover underlying patterns and interactions that are not readily apparent through experimental observations alone. This approach allows us to make more informed generalizations about how each process parameter contributes to fatigue performance, thereby providing a comprehensive understanding of the material's behavior under various manufacturing conditions. Notably, the role of the spatial distribution of pores and its variation as a function of powder pre-processing and additive manufacturing processing parameters will be thoroughly investigated using standard statistics methods in a separate study [28].

2.3.1. Analyzing the relationship between variables using correlation coefficients

The Pearson correlation coefficient measures linear relationships and assumes that both variables are normally distributed. It is highly sensitive to outliers and is used when both variables are continuous and roughly normally distributed.

The Spearman Rank correlation is a non-parametric measure that assesses how well the relationship between two variables can be described by a monotonic function. It ranks the data and then applies Pearson's method to these ranks, making it more robust to outliers and non-normal distributions.

The Kendall Tau correlation coefficient is another non-parametric measure that assesses the ordinal association between two variables. It evaluates the number of concordant and discordant pairs in the data, providing insight into the strength of the ordinal relationship. This makes Kendall Tau particularly useful for small sample sizes and ordinal data.

2.3.2. Analysis of Variance (ANOVA)

ANOVA is a statistical method used to compare means across multiple groups to assess whether there are any statistically significant differences between them. It calculates an F-statistic, which is the ratio of the variance between group means to the variance within the groups. A higher F-value typically indicates a greater probability that there are significant differences among the group means. The p-value (PR) associated with this F-statistic helps in determining the statistical significance. If the p-value is less than the chosen significance level (commonly 0.05), it suggests that the group means are significantly different.

2.3.3. *Tukey Test Applied to ANOVA Results*

The Tukey HSD Test meticulously conducts pairwise comparisons while maintaining control over the type I error rate for multiple comparisons. This step is particularly critical for the pit height R_v variable, where the ANOVA yielded a p-value indicative of highly significant differences, and for the pore count, where distinct comparisons across HIP status are crucial. By providing specific mean differences, confidence intervals, and individual p-values for each pair of means, the Tukey HSD Test offers a stringent statistical confirmation of the differences observed, ensuring the validity of the inferences drawn from the ANOVA.

3. Results

3.1. Microstructure observations

The microstructures of both as-built and HIP-treated samples were examined on sections that included the build direction, i.e., parallel to the BD, as shown in Figure 3. Optical images revealed columnar grains in both samples, indicating the preservation of the as-built grain structure after HIP treatment. This preservation occurred because the heat treatment (900 °C) was conducted below the β transus temperature (995 °C) [29]. The prior β grains, approximately 85±35 μm in width, spanned several millimeters in the as-built sample, similar to our earlier study in [30]. The primary difference in microstructure between the as-built and HIP-treated samples was the segregation of Al and V atoms and the decomposition of martensitic α′ laths into a basket-weave α+β microstructure, as seen in the SEM micrographs in Figure 3. Additionally, thicker and longer α laths formed at the prior β grain boundaries post-HIP treatment. Small rod-shaped β phases appeared in the α phase matrix, alongside the thicker α phase at the prior β grain boundaries. Although the area fraction of grain boundary α is small, it suggests that most β grain boundaries contain it. EBSD analysis confirmed that the basket-weave microstructure and the part's texture remained consistent before and after HIP treatment. Notably, the average width of the α/α′ laths increased slightly from 1.29 μm to 1.68 μm after HIP.

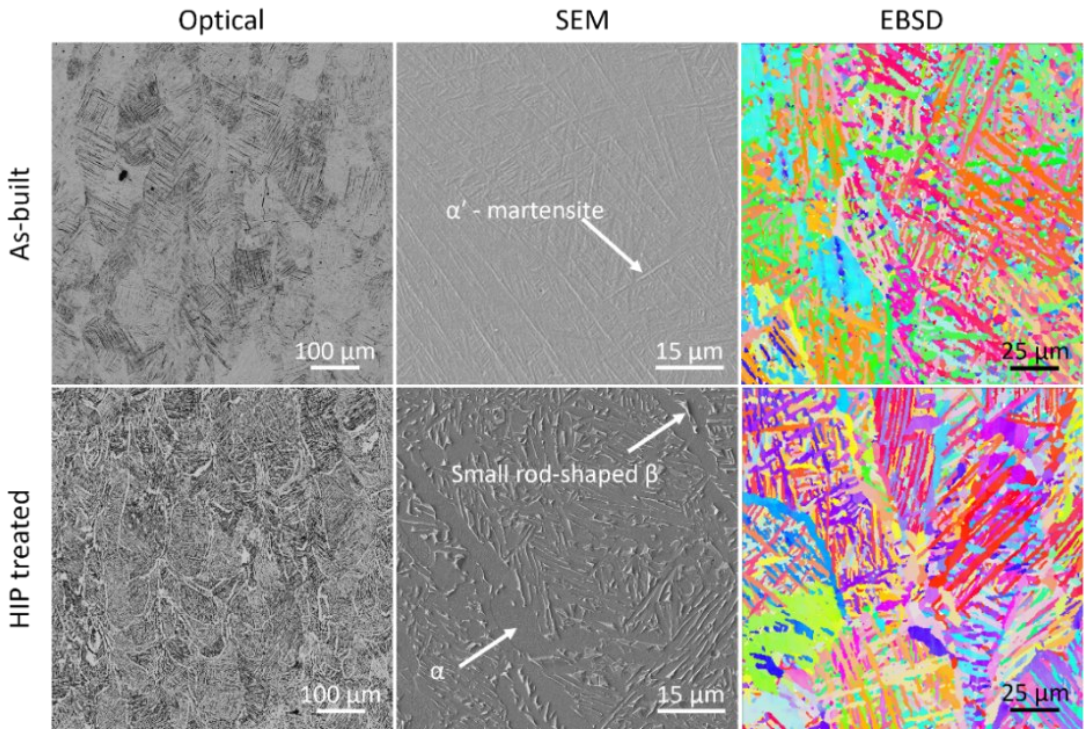

Figure 3. A comparison between microstructure and texture of the as-built and HIP treated L-PBF processed Ti-6Al-4V parts. Optical and SEM-EBSD micrographs showed prior β grains contained α′ lath in the as-built condition while a basket-weave microstructure was seen in the HIP treated sample with a trace amount of grain boundary α phase formation.

3.2. *Pore analysis*

The size, quantity, and spacial distribution of pores were studied using µ-CT, and the results are presented in Figure 4A. Variations were observed based on manufacturing conditions and post-process treatments. Generally, L-PBF parts produced with contouring exhibited a higher pore content in the sub-surface regions (about 200 µm beneath the surface) with larger pores compared to parts made without contouring. When fine particles were L-PBF processed, the sub-surface pore fraction and size were greater than with coarse powder. This was confirmed by pore analysis results for both as-built and HIP-treated samples. Typically, sub-surface pores were connected to the open surface, so HIP treatment did not close them. After HIP treatment, the L-PBF processed fine powder showed a significantly higher fraction of sub-surface pores compared to the coarse powder. However, in regions more than 200 µm from the surface, parts made with fine powder exhibited lower pore content compared to those made with coarse powder.

To eliminate sub-surface pore defects, mechanical grinding was performed on the gauge area of selected samples, removing about 200 µm from the surface. Figure 4B shows pore characteristics based on equivalent diameter and distance from the surface, revealing that surface grinding effectively removed sub-surface defects. Mechanical grinding was particularly effective on HIP-treated specimens. Figure 4C presents probability plots of cumulative pore size

distributions for different sample conditions, while Figure 4D summarizes the effects of the L-PBF process and post-process treatments on pore content and surface finish. Examining pore sphericity as a function of distance from the surface provided insight into how post-processing treatments like HIP and surface grinding impacted pore shape and distribution in Ti-6Al-4V components produced through L-PBF. The findings in Figure 5 indicate that HIP treatment removed pores not in contact with the free surface, but the morphology and quantity of open pores beneath the surface remained unchanged.

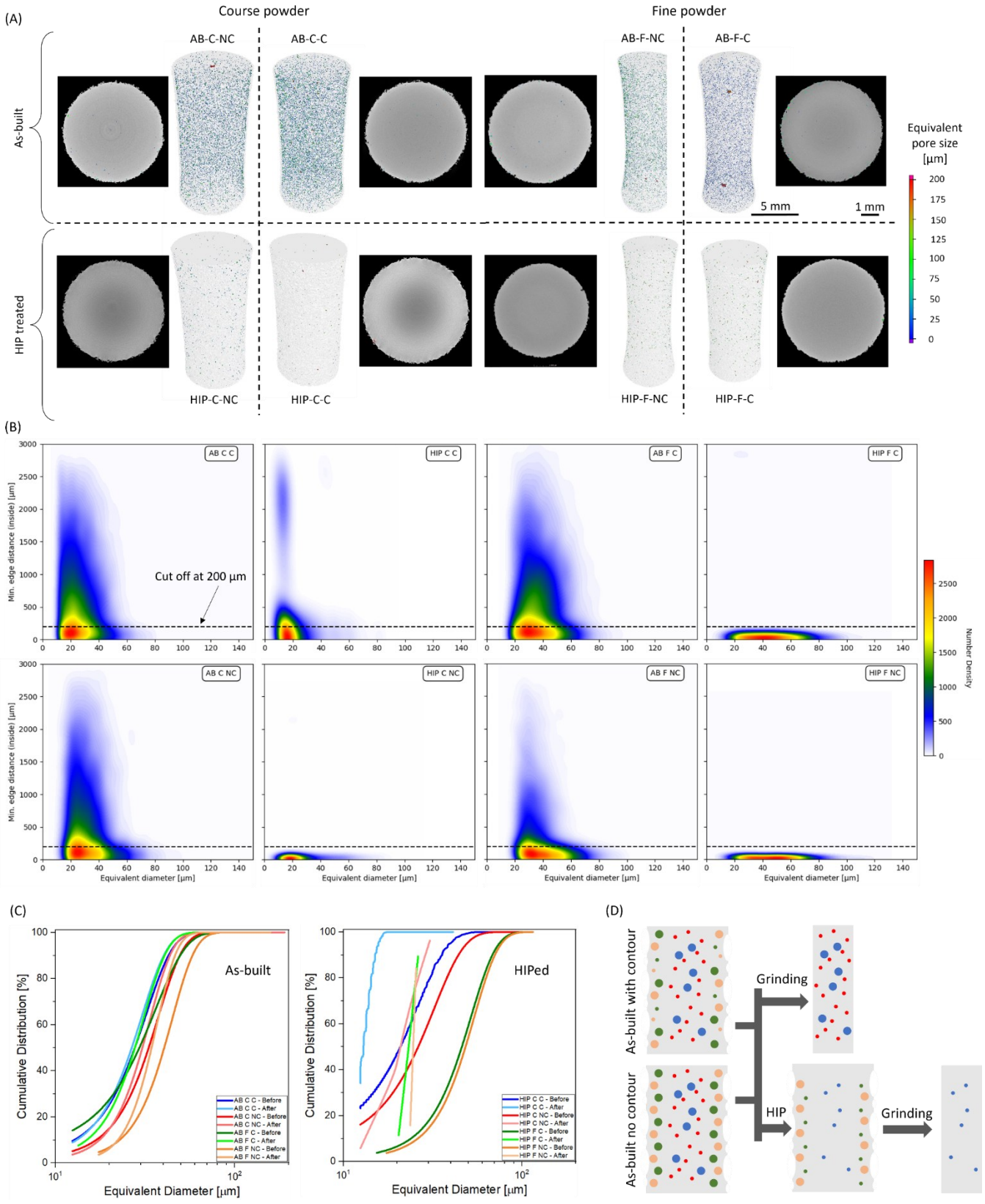
(A)
Course powder
Fine powder
AB-C-NC
AB-C-C
AB-F-NC
AB-F-C
As-built
HIP treated
HIP-C-NC
HIP-C-C
HIP-F-NC
HIP-F-C
5 mm
1 mm
Equivalent pore size [µm]
200
175
150
125
100
75
50
25
0
(B)
AB C C
HIP C C
AB F C
HIP F C
AB C NC
HIP C NC
AB F NC
HIP F NC
Min. edge distance (inside) [µm]
Cut off at 200 µm
Equivalent diameter [µm]
Number Density
(C)
As-built
HIPed
Cumulative Distribution [%]
Equivalent Diameter [µm]
AB C C - Before
AB C C - After
AB C NC - Before
AB C NC - After
AB F C - Before
AB F C - After
AB F NC - Before
AB F NC - After
HIP C C - Before
HIP C C - After
HIP C NC - Before
HIP C NC - After
HIP F C - Before
HIP F C - After
HIP F NC - Before
HIP F NC - After
(D)
As-built with contour
As-built no contour
Grinding
HIP
Grinding

Figure 4. (A) 3D reconstructed µ-CT data from the gauge section of L-PBF processed Ti-6Al-4V powders in various conditions: as-built, HIPed, with or without contour, including a slice of the XY plane. (B) Plots comparing equivalent pore diameter against distance from the surface, with red dashed lines indicating the 200 µm threshold where pores were removed by mechanical grinding. (C) Cumulative pore distribution as a function of equivalent pore diameter. (D) Schematic representation of pore content in different L-PBF processed parts: as-built, HIPed, and mechanically ground conditions. Red, blue, green, and orange colors denote internal small pores, internal large pores, sub-surface pores not connected to the surface, and sub-surface pores connected to the surface, respectively.

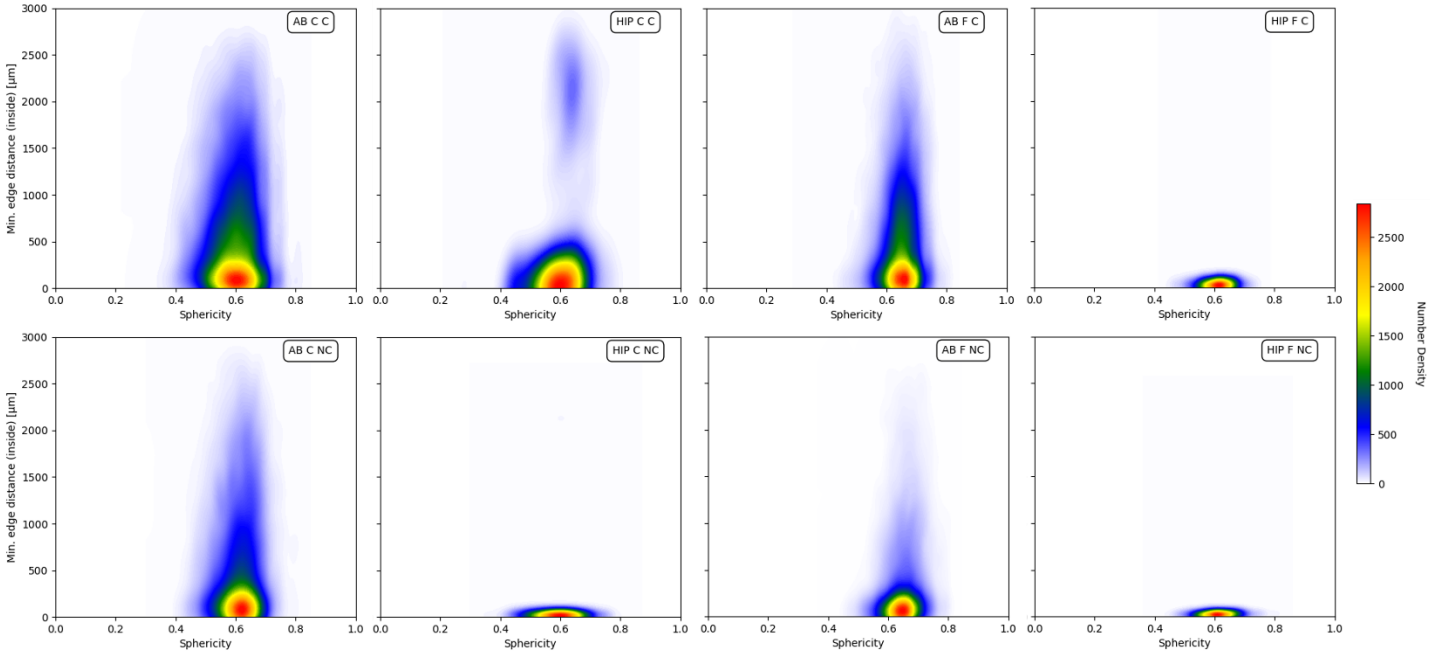

Figure 5. Analysis of pore sphericity against pore distance from surface in the L-PBF processed Ti-6Al-4V powder. Data was extracted from the reconstructed µ-CT data shown in Figure 4A.

3.3. *Surface topology observations and surface roughness analysis*

Surface roughness data, obtained by optical profilometry from the gauge section of fatigue samples, is presented in Figure 6. The results indicate that contouring consistently led to reduced surface roughness (R_a) and smaller pit height (R_v), as shown in Figure 6C and Figure 6D. This effect was particularly pronounced when fine powder was used in the L-PBF process for manufacturing Ti-6Al-4V parts. Additionally, HIP treatment lowered surface roughness irrespective of powder particle size or contouring. The data for both R_a and R_v show considerable variability, highlighted by the standard deviation in the plots. This underscores the importance of taking multiple measurements to accurately capture surface roughness parameters, reflecting the significant variation in surface conditions and measurement methods.

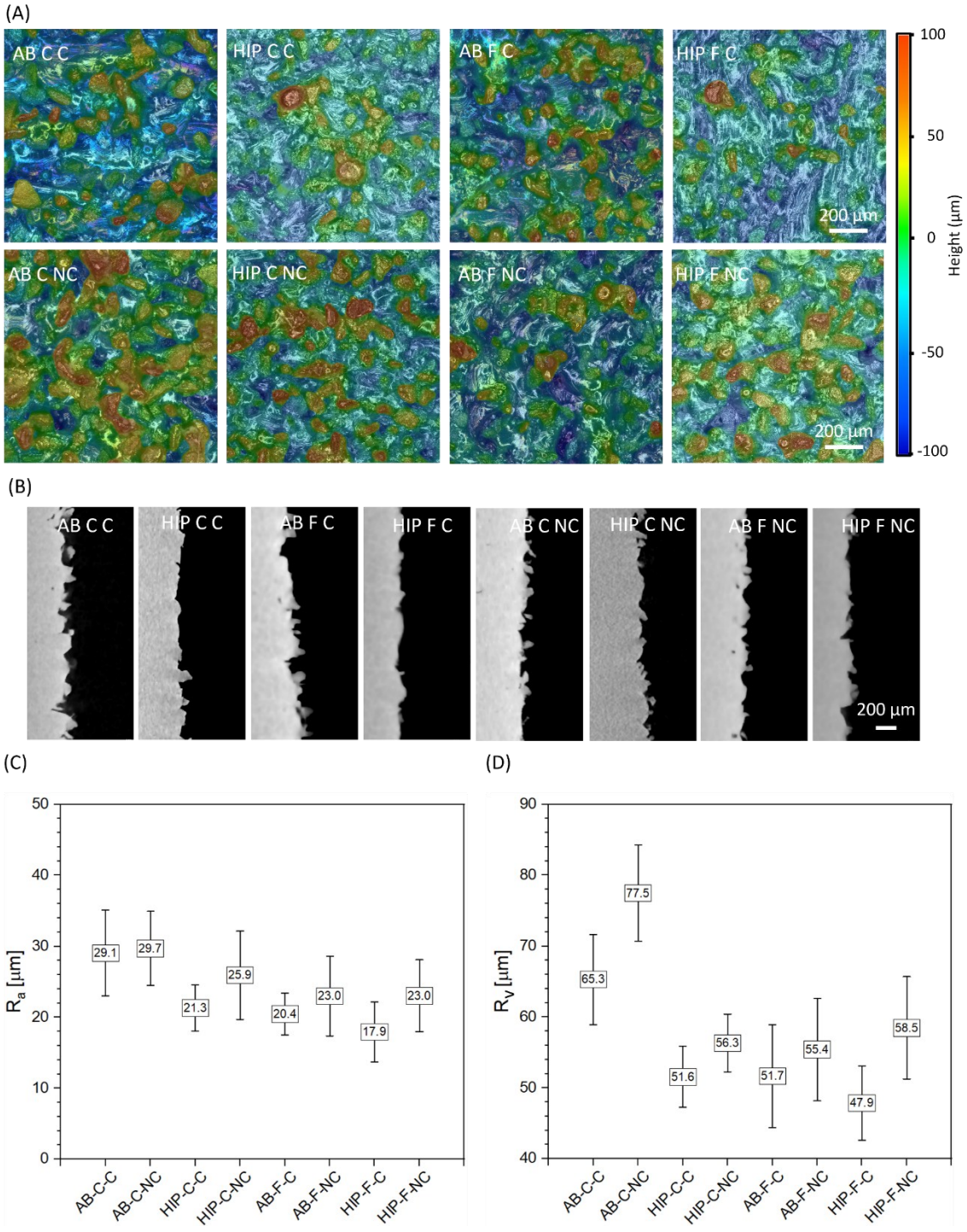

Figure 6. (A) Optical surface profilometry micrographs, (B) Cross-section micrographs from µ-CT data showing roughness and micro-notches at the surfaces, (C) surface roughness, R_a, and (D) the maximum valley or pit height, R_v, data collected from the gauge section of fatigue samples under different manufacturing conditions including as-built, HIP treatment, and mechanical griding.

3.4. *Fatigue life results*

The fatigue performance of L-PBF processed Ti-6Al-4V parts is shown in Figure 7. Each dataset is fitted to the Basquin equation, represented by solid lines for coarse powder and dashed lines for fine powder, as detailed in section 4. The study examined the effects of powder size (fine vs. coarse), L-PBF process variations (with or without contouring), and post-process treatments (HIP and/or mechanical grinding) on fatigue performance.

Figure 7A compares the fatigue performance of Ti-6Al-4V samples produced with fine and coarse powders in both as-built and mechanically ground states. Components made from fine powders exhibited slightly better fatigue life compared to those from coarse powders under similar stress conditions. Surface grinding improved fatigue life for both fine and coarse powder parts, attributed to reduced surface roughness below 0.2 μm [15], which eliminated potential crack initiation sites present in the as-built components.

Figure 7B shows that omitting contouring did not significantly impact the fatigue performance of the L-PBF processed parts, causing only a slight reduction in fatigue life in the high-cycle region. Although contouring slightly reduced surface roughness, μ-CT data in Figure 4 and Figure 5 indicated an increase in the size and number of sub-surface pores, negatively affecting fatigue life. Regardless of powder size, parts made with non-spherical Ti-6Al-4V powder showed similar fatigue performance to those made with spherical powder. However, even with mechanical grinding, these samples exhibited lower fatigue resistance compared to conventionally wrought Ti-6Al-4V parts.

Figure 7C illustrates the combined effect of HIP and mechanical grinding on the fatigue performance of L-PBF processed Ti-6Al-4V parts made from non-spherical powders. HIP-treated samples, regardless of powder size, showed similar fatigue performance to as-built samples. After HIP treatment, the influence of particle size was negligible, with nearly identical fatigue performance observed across different sizes. The low-cycle fatigue region remained unchanged, while there was a slight improvement in the high-cycle fatigue region, likely related to sub-surface pore defects.

Mechanical grinding had a more pronounced impact on the HIP-treated samples. The combination of HIP and mechanical grinding significantly enhanced the fatigue performance of components made from non-spherical powder. Consequently, parts processed from fine powder, followed by HIP treatment and surface grinding, achieved fatigue performance nearly equivalent to wrought samples.

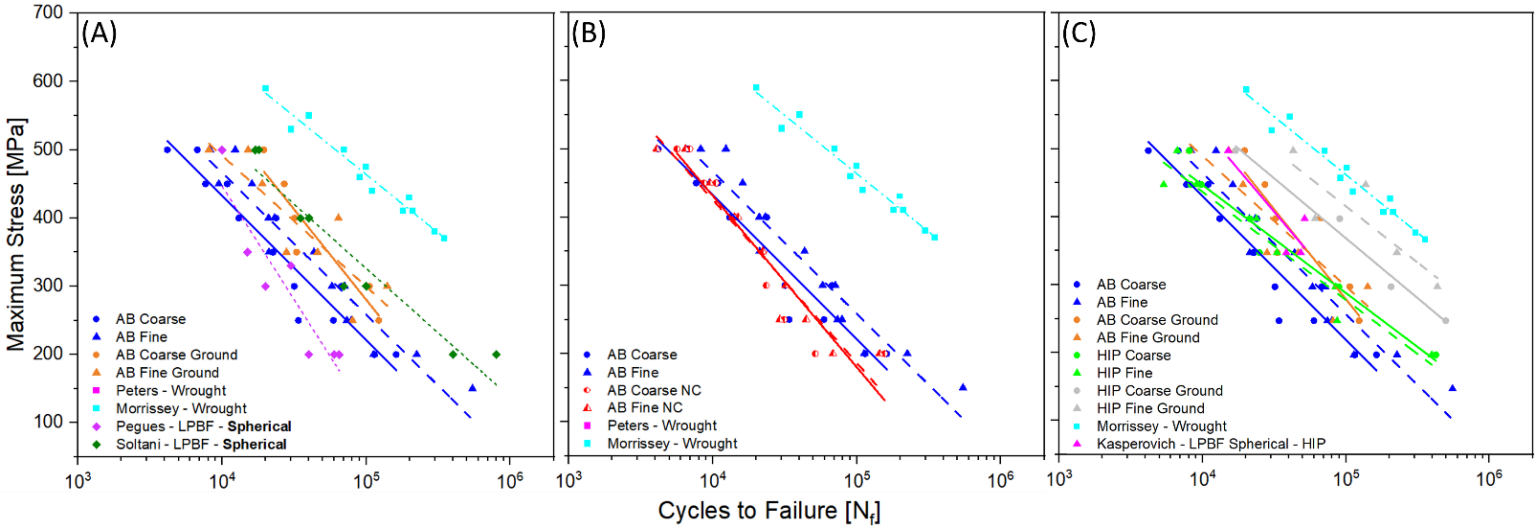

Figure 7. Fatigue performance of L-PBF processed Ti-6Al-4V using fine and coarse non-spherical powders is shown in (A) as-built and surface ground conditions, (B) as-built conditions with and without contouring, and (C) as-built, HIP-treated, and mechanically ground conditions. Fatigue data for wrought samples (including machined surface) and L-PBF processed samples using spherical powder were sourced from the literature [31–35]. Each line, fitted to the Basquin equation, represents an experimental data set, with solid lines for coarse powder and dashed lines for fine powder.

3.5. Fractography

Fracture surfaces at stress amplitudes of 250 and 500 MPa from L-PBF processed parts using non-spherical fine powders are shown in Figure 8. Samples with as-built surface conditions, regardless of HIP treatment, failed exclusively at surface micro-notches. Conversely, mechanically ground samples exhibited crack initiation at sub-surface defects such as pores, indicating that cracks did not necessarily start at the surface. The optical micrographs revealed four distinct regions on the fracture surface corresponding to different stages of fatigue crack initiation and growth: (1) crack initiation site, (2) quasi-stable crack growth region, (3) unstable crack growth region, and (4) final rupture region due to stress overload. Notably, the final rupture region decreased in size as the stress amplitude decreased. Additionally, the number of crack initiation sites on as-built surface samples decreased with lower stress amplitudes. Mechanically ground samples typically showed only one crack initiation site, either a surface-exposed pore due to grinding or a sub-surface pore close to the surface. None of the samples exhibited internal defects as crack initiation sites.

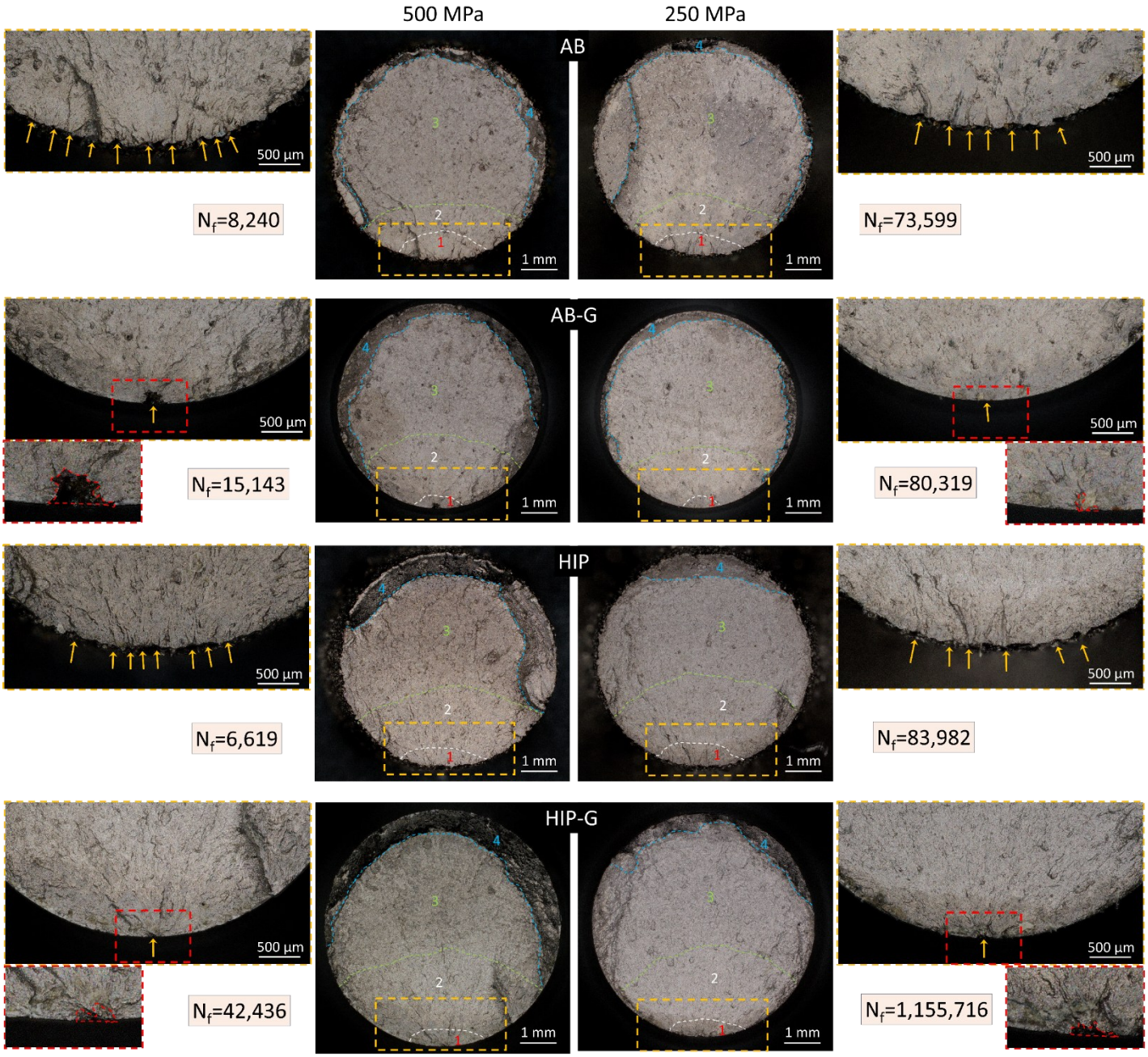

Figure 8. Optical micrographs showing fracture surfaces from the L-PBF processed non-spherical Ti-6Al-4V fine powder tested under 250 and 500 MPa, showing the crack initiation sites in higher magnification. Different stages of crack initiation and growth were recognized using dashed lines including (1) the crack initiation sites and stable crack propagation, (2) a quasi-stable crack propagation, (3) unstable crack propagation, and (4) finally, as the stress concentration enhanced associated with the reduction of surface area, rupture took place. In the mechanically ground samples, crack nucleation occurred mainly at the sub-surface pore. Yellow arrows show crack initiation sites.

3.6. X-ray diffraction

To further explore the impact of post-processing treatments on the fatigue performance of L-PBF-manufactured Ti-6Al-4V components, we conducted XRD analysis on selected samples, with a specific focus on those fabricated using fine powder. The results, illustrated in Figure 9, revealed notable findings through quantitative XRD analysis utilizing the MAUD software and Rietveld refinement method [27]. Additionally, micro-strain (ε) values were calculated for these samples [36] (using the equation given in the Table 3), and the results are presented in Table 3.

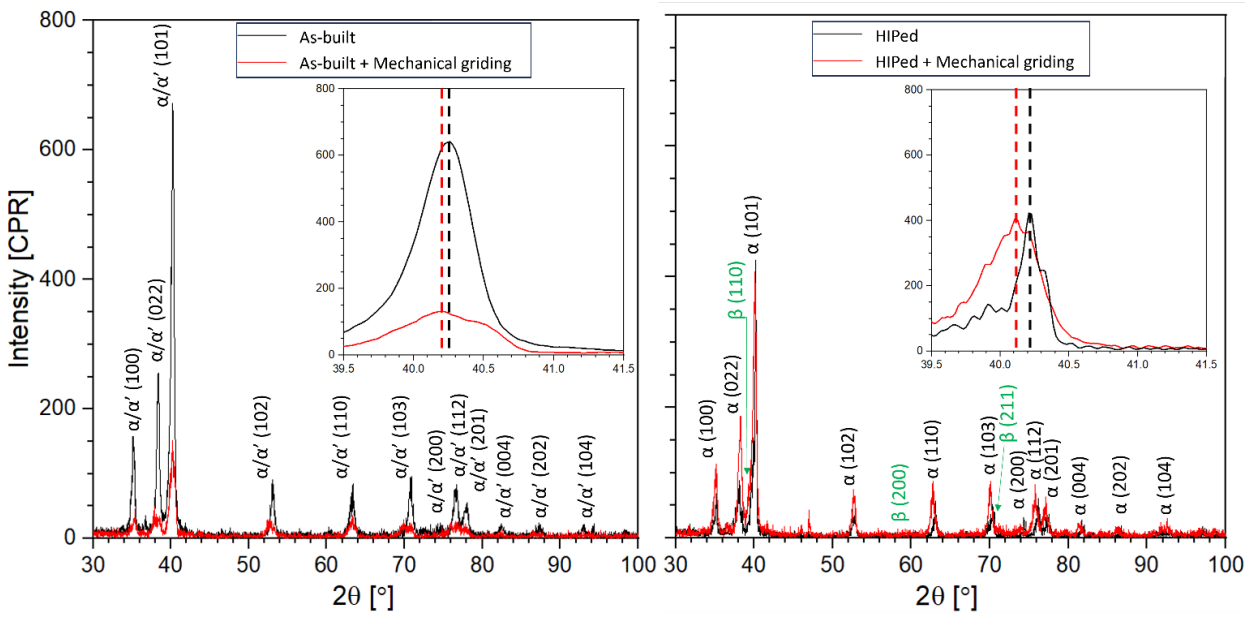

Figure 9. X-ray diffraction pattern data from the L-PBF processed fine Ti-6Al-4V powder in the as-built, HIPed, and mechanically ground conditions. The inset figure shows the peak shift at 40°, the black dashed line and the red dashed line indicate the peak center of the as-built and mechanically ground conditions, respectively.

Table 3. Analyzing crystallographic parameters in L-PBF processed fine Ti-6Al-4V powder: A Comparison between as-built, HIPed, and mechanically ground specimens.

	α/α′ (101)				α/α′ (102)				α/α′ (110)			
	2θ [°]	d-spacing [Å]	FWHM [°]	ε* [%]	2θ [°]	d-spacing [Å]	FWHM [°]	ε [%]	2θ [°]	d-spacing [Å]	FWHM [°]	ε [%]
As-built (AB)	40.22	2.240	0.506	0.046	53.07	1.724	0.516	0.064	63.29	1.468	0.643	0.099
AB + Mechanically Ground	40.20	2.241	0.749	0.069	52.76	1.734	1.175	0.148	63.24	1.469	0.978	0.151
HIP	40.21	2.241	0.239	0.022	53.01	1.726	0.494	0.062	63.20	1.470	0.518	0.080
HIP + Mechanically Ground	40.19	2.242	0.518	0.047	52.67	1.736	0.627	0.078	63.10	1.472	0.551	0.085

* $\varepsilon = \frac{\beta}{4}\sin\theta$, in which β is the FWHM of the peak and θ is the Bragg angle of the (hkl) reflection.

4. Discussion

The fatigue performance of L-PBF parts using non-spherical Ti-6Al-4V powders was influenced by several key factors: (i) the high surface roughness, with surface intrusions acting as potential crack initiation sites [37], (ii) internal defects, especially in the sub-surface regions, which served as stress concentrators and adversely affected fatigue performance [38], (iii) the martensitic microstructure resulting from the rapid cooling rates of the L-PBF process [39], and (iv) the directional grain growth oriented along the build direction [40]. These factors are ranked from most to least impactful. This study evaluates the effects of each parameter (powder morphology, powder size, contouring, HIP, and mechanical grinding) based on these considerations.

4.1. Analysis of fatigue limit using Basquin equation

To better compare the fatigue life of the L-PBF processed Ti-6Al-4V samples under different conditions, the Basquin equation [41] is used which correlates the fatigue stress amplitude (σ_a) to the cycles to failure (N_f) by using fatigue strength coefficient (σ'_f) and fatigue strength exponent (b). The following equation is fitted to each set of experimental data as shown in Figure 7:

$$\sigma_a = \sigma'_f(2N_f)^b \quad (1)$$

Based on the Basquin equation, which is typically used for high-cycle fatigue, for a given σ'_f, smaller values of b correspond to a shallower slope and therefore higher fatigue limit. The Basquin equation was used to fit a line on the fatigue data in the current study as well as data from literature and the results are summarized in Table 3.

By choosing a fixed number of cycles to failure (*e.g.*, N_f= 1000), the fatigue strength at that cycle (σ'_3 for N_f= 1,000 or σ'_5 for N_f= 100,000) was extracted to compare fatigue behavior under different conditions. Based on the calculated data (shown in Table 3), the AB-C-G sample had the highest fatigue strength at 1000 cycles, however, the large b value of this sample revealed a strong dependence on stress amplitude, which was not desirable. Moreover, HIPing resulted in smaller σ'_3 value which can be attributed to the increase in ductility and decrease in strength of the samples because of the decomposition of α' martensite to α+β. The σ'_5 values show that the HIP-F-G sample had the highest fatigue strength at 100,000 cycles which was because HIPing closed almost all the internal pores, and the mechanical grinding process eliminated the sub-surface pores, thus, drastically increasing the fatigue strength of the sample.

Table 4. The calculated fatigue strength coefficient (σ'_f), fatigue strength exponent (b), fatigue strength at 1,000 cycles (σ'_3), and fatigue strength at 100,000 cycles (σ'_5) of the L-PBF processed non-spherical Ti-6Al-4V powder in different conditions.

	σ'_f [MPa]	b	σ'_3 [MPa]	σ'_5 [MPa]	Microstructure	Pore density [#/100 mm^3]
AB C C	5743	-0.2623	782	233.6	α′	24410
AB C NC	14113	-0.3526	968	190.7	α′	13052
AB F C	8609	-0.29	953	250.7	α′	28564
AB F NC	8228	-0.3	841	211.3	α′	15191
HIP C C	3647	-0.21	735	278.2	α+β	846
HIP F C	3097	-0.20	688	276.2	α+β	660
AB C G	17386	-0.34	1318	276	α′	15917
AB F G	2401	-0.16	816	303.5	α′	6471
HIP C G	3989	-0.20	891	359.3	α+β	560
HIP F G	3610	-0.18	936	413.1	α+β	3
Pegues	66756	-0.50	782	149.3	α′	n/a
Soltani	12073	-0.30	968	310.1	α′	n/a

4.2. Effect of powder characteristics on fatigue life

The effect of powder morphology on the fatigue performance of L-PBF processed Ti-6Al-4V components was dominated by how each powder morphology influences the final surface roughness of the parts. Typically, the surface roughness observed in metal powder additive manufacturing components is attributed to (i) the presence of partially or incompletely melted powder (on vertical or downskin surfaces), and (ii) the creation of menisci, such as surface waviness, on exposed surfaces [42]. The characteristics of the starting powder are widely recognized for their significant impact on surface finish attributes [37,43–46]. Specifically, factors such as powder shape, size, and distribution play a critical role in determining laser absorption characteristics, consequently affecting surface texture. It is inferred that finer powder results in smoother surfaces; nonetheless, the spreading of finer powders poses greater challenges due to issues such as agglomeration [46]. Conversely, larger powder particles may be easier to spread but impose limitations on surface quality due to minimum feature size and minimum layer thickness constraints [46]. Sendino *et al*. [47] reported that the size of the powders adhering to the surface corresponded to the dimensions of the smallest particles within the used powder feedstock. This was because smaller particles were more prone to experiencing partial melting at the layer contours due to the heat transfer between the molten material and the powder bed. The fatigue results of the as-built samples in this study are in line with those for samples manufactured with spherical powder. Pegues *et al*. [35] investigated the fatigue performance of Ti-6Al-4V parts fabricated at a 45° angle from the substrate using various build geometries and surface roughness levels. When

comparing their fatigue results with those from the current study, it was found that samples made with non-spherical powder exhibited slightly better performance, irrespective of powder size distribution. This improvement was attributed to the rougher down-skin region compared to the up-skin region, leading to non-uniform surface roughness in their samples.

4.3. Effect of powder size distribution on fatigue life

The fatigue life of samples made with coarse powder was consistently lower than those made with fine powder (see Figure 7A). This difference is attributed to the impact of powder size distribution on surface roughness, as illustrated in Figure 6. L-PBF processed parts using coarse powder (AB-C-C) had an R_a of 29.1 μm and R_v of 58.5 μm, whereas parts using fine powder (AB-F-C) had an R_a of 20.4 μm and R_v of 51.6 μm. The increased surface roughness with coarse powder was due to the presence of larger partially melted particles on the surface [48]. In contrast, Soltani *et al.* [34] used spherical powder with an average diameter of 34 μm to fabricate Ti-6Al-4V parts via L-PBF, achieving slightly better fatigue results than the current study due to the smaller powder size (fine powder: 50-120 μm, coarse powder: 75-175 μm) leading to reduced surface roughness and improved fatigue performance. Mechanical grinding significantly enhanced fatigue performance by removing surface roughness, making the fatigue performance of samples from both fine and coarse powders comparable and mitigating the initial effects of powder size distribution.

Recent research conducted by Kantzos *et al*. [37] found that the hotspot features on the as-built surface remained consistent, regardless of whether fine or coarse Ti-6Al-4V powder was used. This suggests that surface roughness is more sensitive to build conditions than variations in particle size. In other words, the adhering particles have no effect on stress concentration, and it is the valleys that matter. The feedstock powder characteristics, such as size, likely have a limited impact on the performance of metal AM parts with rough surfaces. This is primarily because near-surface pore has a more significant influence on localized damage in specific surface regions [49] compared to surface roughness [37]. A minimal effect of powder size on fatigue performance was also reported by Gockel *et al*. [44], where it was found that the average powder particle size in the raw material affected the roughness parameter R_a but had little influence on fatigue performance.

4.4. Effect of contouring on fatigue life

Contouring is generally employed to enhance the surface quality and geometric precision of L-PBF processed parts [50]. However, it introduces complexities such as spattering and balling in metal additive manufacturing, resulting in partially sintered particles and micro-notches that contribute to rough surface features [37,49,51]. Additionally, contour regions can become sites for non-steady-state defects like end-of-track and turnaround pores [38]. Complex thermal histories in these areas, as documented in several studies [52–56], can lead to keyhole pores. Consequently,

surface defects in powder bed AM present a multifaceted challenge that requires further investigation.

Mishurova et al. [57] demonstrated that contouring reduced the surface roughness of L-PBF processed Ti-6Al-4V alloy from 33.3 μm to 13.2 μm. However, improper contouring parameters can lead to excessive heat source penetration, creating new pores and reducing geometric precision, or insufficient penetration, failing to eliminate defects and improve precision. Karimialavijeh et al. [58] found that increasing the laser scan speed during contouring reduced sub-surface pores but increased surface roughness, negatively impacting fatigue life. Bonesso et al. [59] showed that the effect of contouring on surface roughness depends on the initial powder particle size distribution. For example, contouring did not change the surface roughness significantly for larger powders but drastically improved it for smaller powders. This effect was also observed in the current study, where fine powders showed a notable reduction in surface roughness with contouring (no contour: 23 μm, contour: 20.4 μm) compared to coarse powders (no contour: 29.7 μm, contour: 29.1 μm) as seen in Figure 6. Therefore, it is reasonable to further investigate the impact of contouring on the fatigue life of L-PBF processed non-spherical powders by examining its effect on surface roughness.

Another consequence of contouring is its impact on the shape and distribution of pores, particularly in the sub-surface region, as shown in Figure 4B and Figure 5. Without contouring, sub-surface pores tend to be more spherical, whereas contouring leads to elongated pores. This elongation is likely due to the contouring process parameters, which can eliminate keyhole pores formed during normal hatch scanning but create lack-of-fusion pores. Additionally, spattering during contouring can cause spatters to fall onto the sample, resulting in lack-of-fusion pores in subsequent layers. Given the variability in contouring parameters, such as laser power and scan speed, it cannot be considered a fixed solution and warrants further study.

4.5. Effect of HIP treatment on fatigue life

The L-PBF process typically entails the presence of internal defects, which, while manageable, are essentially unavoidable. To address this issue and achieve the highest possible relative density, a high pressure, high temperature process known as HIP was suggested [60]. Numerous investigations found no flaws in their samples following HIPing when employing μ-CT [61]. Nevertheless, this outcome might be attributed to the limited resolution of the imaging process used. In the current study, we adopted a similar approach to mitigate internal pores and improve the fatigue performance of L-PBF-manufactured Ti-6Al-4V parts. While the HIP process effectively eliminated a significant portion of the internal pores, it had minimal impact on sub-surface pores, particularly those linked to the surface. Additionally, HIP resulted in a reduction in surface roughness, although this reduction was primarily numerical in nature. The process did not alter the surface intrusions but rather flattened or rounded them, leading to the observed decrease in surface roughness. The reduction in surface roughness, achieved by eliminating the extrusions,

does not have an impact on fatigue life since only the intrusions serve as crack initiation sites. This explains why the fatigue life of the HIP samples was comparable to that of the as-built samples. Gunther *et al*. [62] showed the same behavior in L-PBF processed Ti-6A-4V parts under fatigue testing before and after HIP treatment. They showed that in the as-built surface condition, the samples had comparable fatigue lives regardless of the application of HIP process and surface defects were the main reasons for fatigue failure, specifically, in the high stress region.

4.6. Combining post-process treatments on fatigue life

Most issues affecting the fatigue life of L-PBF processed parts can be addressed by eliminating surface roughness, which almost invariably improves fatigue life. While defects significantly impact fatigue performance during extended lifespans due to decreased localized plastic deformation, other issues such as internal pores, microstructure, and texture persist even after surface roughness removal [63]. Combining HIP with mechanical grinding can mitigate nearly all these problems.

First, HIP transforms the microstructure of L-PBF processed Ti-6Al-4V parts from predominantly martensitic to a more ductile lamellar α+β structure, enhancing fatigue life [20], as demonstrated in Figure 3. Second, mechanical grinding eliminates surface defects, most sub-surface defects, and induces compressive residual stress near the surface, further increasing fatigue life. For instance, comparing the σ'_5 values of AB-F-G (303 MPa) and HIP-F-G (413 MPa) samples shows a significant improvement in fatigue life. This combination has proven highly effective in our study, bringing the fatigue life of L-PBF processed Ti-6Al-4V parts close to that of wrought parts.

The primary factor preventing these parts from achieving the same fatigue performance as wrought parts is the presence of texture [20]. While the HIP process decomposes the α′ phase into α+β phases, it does not alter the orientation and morphology of primary β grains. Columnar prior β grains containing grain boundary α are still present after HIP (as shown in Figure 3), but they are less brittle than in the as-built samples.

4.7. Relationship between variables using correlation coefficients

Figure 10A showed the results of correlation coefficient analysis. The calculated correlation coefficients are consistent between the three methods including Pearson, Spearman, and Kendall Tau. It can be concluded that there is a strong anti-correlation between R_v and contour as well as pore count and HIP variables. Also, fatigue strength exponent and contour variables show some positive correlations.

To further investigate the relationships between variables, ANOVA was employed to assess the consistency of observed correlations across distinct groups. Plots in Figure 10B provided evidence of statistically significant differences between group means for the variables under consideration. For the fatigue strength exponent variable, the p-value is 0.04999, which is

marginally below the conventional alpha level of 0.05, suggesting that there are significant differences between at least two of the group means for contour. The p-value for the R_v variable is extremely low (p-value < 0.00001), indicating strong evidence against the null hypothesis of equal means across the contour groups. For pore count, the p-value of 0.00049 also signifies that the group means are significantly different when comparing HIP statuses. The central tendency and dispersion represented by the box plots affirm these findings, with notable differences in medians and interquartile ranges among the groups, particularly for R_v and pore count.

The pairwise comparison among the group means for the variables fatigue strength exponent vs contour, R_v vs contour, and pore count vs HIP are shown in Figure 10C. For fatigue strength exponent variable, the non-overlapping confidence intervals among the groups highlight statistically significant differences between each pair of group means when compared across contour levels. In the case of R_v, the magnitude of the differences between groups is considerable, as evidenced by the length of the confidence intervals, which do not overlap with zero, indicating significant differences. Regarding pore count vs HIP, the confidence intervals again suggest significant differences between the groups, with no overlap, thus confirming the presence of distinct group effects. These results confirm the ANOVA findings by clearly showing the significant differences between groups, thus strengthening the evidence for our conclusions.

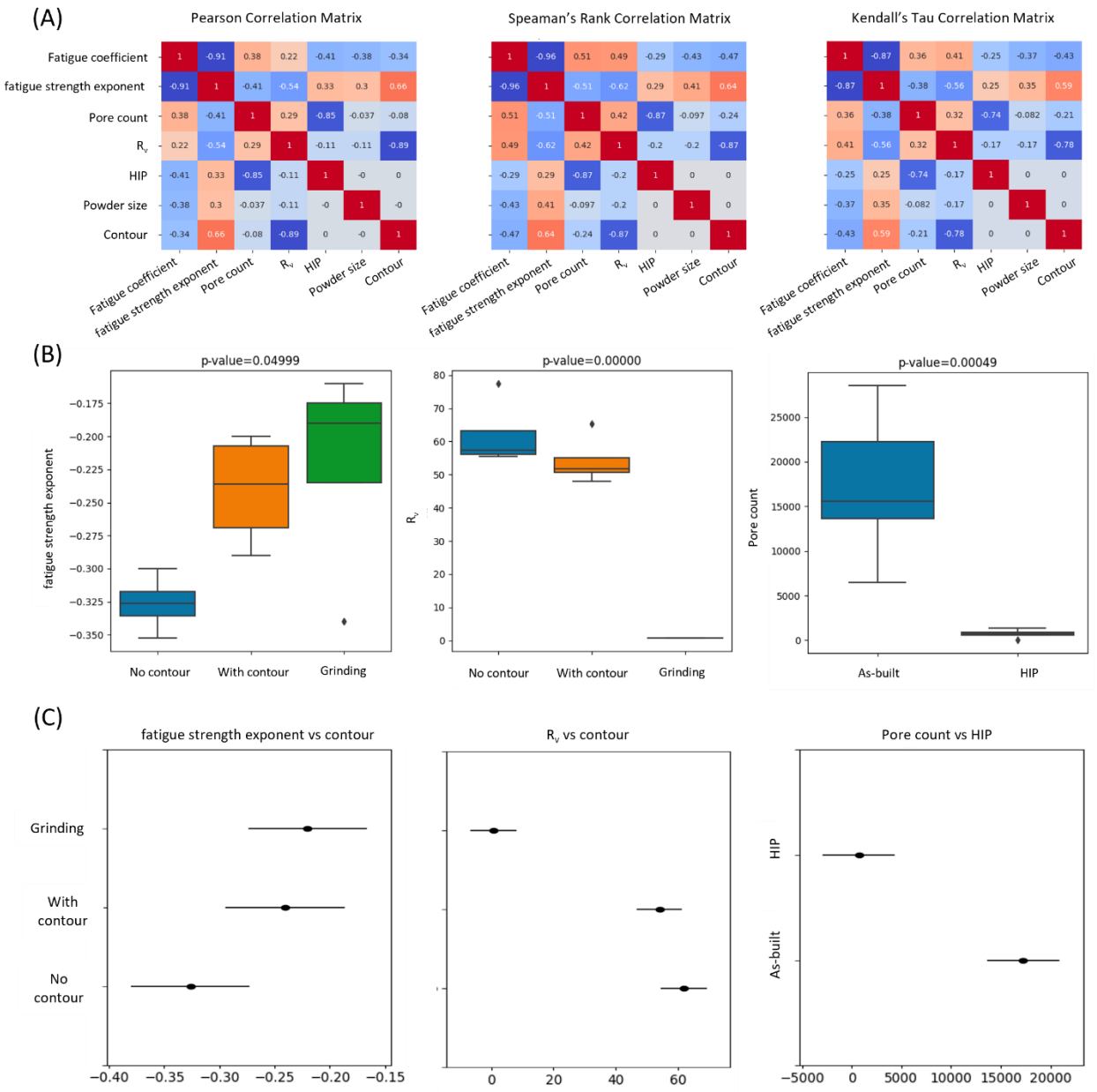

Figure 10. (A) Correlation coefficient analysis, (B) ANOVA analysis results for the correlated variables determined in "A", and (C) Pairwise Comparison Confidence Intervals from Tukey's HSD Test.

4.8. Quantitative analysis of surface residual stress using X-ray diffraction

Through X-ray diffraction analysis perpendicular to the stress axis in fatigue testing, we observed (i) broadening of peaks based on the full width at half maximum (FWHM) in the mechanically ground specimens and (ii) slight shifts in peak positions toward smaller 2θ values. For instance, in the as-built specimens, the {101} plane of the α′ phase exhibited a peak shift from

40.22° to 40.20° after mechanical grinding. This shift signified an expansion of the lattice structure in the direction perpendicular to the plane (elastic out-of-plane lattice expansion), while simultaneously indicating compression within the plane. This was evident from the increase in the d-spacing related to {101}, which increased from 2.240 to 2.241 Å, as determined through Bragg's law. The ε values for the tested samples demonstrated that when mechanical grinding was applied to the as-built specimens, the values of microstrain increased from 0.046 % to 0.069 %, suggesting the possible presence of compressive residual stress. This same trend was observed in the HIPed and surface-treated specimens. According to refs. [15,64], it is noteworthy that the presence of compressive residual stress is associated with the inhibition of crack initiation and improvement in fatigue endurance.

4.9. Critical defect size analysis

The effect of defect size on the fatigue performance of L-PBF processed Ti-6Al-4V parts was investigated, considering factors such as powder characteristics, contouring during the L-PBF process, HIP treatment, and post-surface treatment. The impact of these factors on critical defect size is shown in Figure 11. The methodology introduced by Sanaei and Fatemi [40] was used to measure the average critical defect size in the samples. As expected, the as-built samples exhibited critical defects predominantly as surface defects or micro-notches. In contrast, the mechanically ground samples revealed critical defects mainly in the internal or sub-surface regions. However, mechanically ground samples had internal defects that extended to the surface, serving as crack initiation points.

These observations clarify why crack initiation predominantly occurs on the surface of as-built samples, regardless of HIP treatment or contouring. After removing surface roughness through mechanical grinding, crack initiation was not solely linked to surface defects. In most samples, the crack initiation site was one of the internal defects in the sub-surface region. Another noteworthy observation from the Murakami plot [65] in Figure 11 was that cycles to failure increased as the critical defect size decreased. This aligns with existing literature [62,66,67], which indicates an inverse relationship between average critical defect size and the fatigue life of parts.

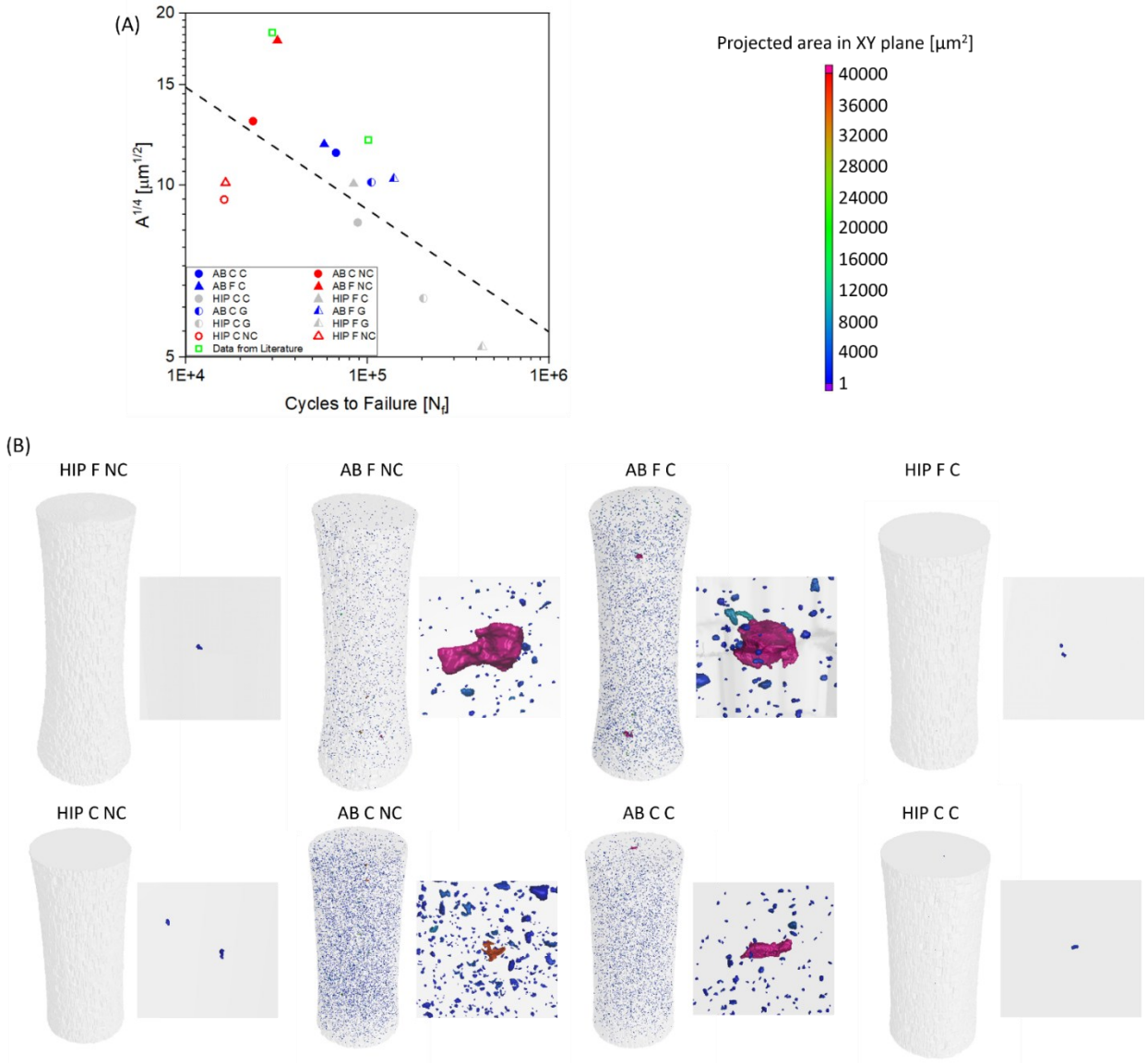

Figure 11. (A) The relationship between average critical defect size and the number of cycles to failure for L-PBF processed Ti-6Al-4V using non-spherical fine and coarse particles under various conditions, including as-built and post-processed treatments, is shown. The samples were tested under a stress amplitude of 300 MPa, with additional data sourced from references [62,66]. (B) µ-CT data analysis highlighting pore defects with the largest projected area in the XY plane across different sample conditions. Clarification: the color bar is for subfigure B.

4.10. Quantification of the surface notch effect

An empirical quantitative method is available to establish a correlation between the fatigue endurance of a sample with surface notches (such as as-built samples with micro-notches) and a sample without surface notches (such as mechanically ground samples). This relationship can be determined using the fatigue notch factor and the following equation [68]:

$$\sigma_{e1} = \frac{\sigma_{e2}}{\overline{K_f}} \quad (2)$$

where σ_{e1} and σ_{e2} refer to the fatigue endurance with or without notches, respectively, and $\overline{K_f}$ is the fatigue notch factor. To calculate the fatigue notch factor $\overline{K_f}$, the elastic stress concentration factor $\overline{K_t}$ and the materials sensitivity to notches q can be used as follows which was adapted from Arola-Ramulu [69]. This model was selected for the output data from this analysis for comparison with the literature.

$$\overline{K_t} = 1 + n(\frac{R_a}{\bar{\rho}_{10}})(\frac{R_t}{R_{zISO}}) \quad (3)$$

$$q = \frac{1}{1+\frac{\gamma}{\bar{\rho}_{10}}} \quad (4)$$

$$\overline{K_f} = 1 + q(\overline{K_t} - 1) \quad (5)$$

where $n = 2$ for tension, γ refers to the average α/α′ lath width, and R_a, $\bar{\rho}_{10}$, R_t, and R_{zISO} refer to the average roughness, average 10-point valley radii, maximum peak-to-valley roughness, and 10-point height roughness, respectively. The following equations were used to calculate values of R_a, R_t, R_{zISO}, and $\bar{\rho}_{10}$ [70]:

$$R_a = \frac{1}{n}\sum_1^n ABS(Z_i - Z_{mean}) \quad (6)$$

$$R_t = ABS(Z_{max} - Z_{min}) \quad (7)$$

$$R_{zISO} = \frac{1}{n}[\sum_1^n ABS(Z_i - Z_{max}) + \sum_1^n ABS(Z_i - Z_{min})] \quad (8)$$

$$\bar{\rho}_{10} = \frac{1}{n}\sum_1^n \rho_{i-min} \quad (9)$$

where Z_i is the height in each point, Z_{max} is the maximum peak height, Z_{min} is the minimum valley depth, and ρ_{i-min} is the deepest valleys' radii. As an example, Figure 12 showed the measurements of two deepest valleys (i.e., ρ_{i-min}) used in the notch factor calculation. For an ideal sinusoidal surface, Arola-Ramulu [69] suggested that the $\frac{R_t}{R_{zISO}}$ ratio would be 1, thus, the $\overline{K_t}$ is dependent on the $\frac{R_a}{\bar{\rho}_{10}}$ ratio. Moreover, to describe the sinusoidal nature of the $\overline{K_t}$, the R_a can be taken as the wave amplitude and the $\bar{\rho}_{10}$ taken as the wave period. The parameters calculated for samples under various conditions are presented in Table 4. Pegues et al. [71] reported a fatigue notch factor of 4.42 for L-PBF processed spherical Ti-6Al-4V powder. In this study, however, all recorded fatigue notch factor values are below 4.42. This indicates that non-spherical powder results in parts with improved fatigue endurance and a lower susceptibility to fatigue failure.

In the present study, if we consider the fatigue notch factor and fatigue endurance limit of the mechanically ground fine HIP sample (HIP-F-G) as 1 (indicating no micro-notches on the surface)

and 350 MPa (see Figure 7), respectively, the calculated (using Eq. 2) fatigue endurance of the same sample before mechanically grinding would be 151.5 MPa. This calculated value was notably close to the experimental measured value of 150 MPa. Furthermore, it is worth noting that all the HIP samples exhibited a lower fatigue notch factor in comparison to their as-built counterparts. This indicates the beneficial effect of the HIP process in diminishing the influence of surface roughness on the fatigue endurance of the samples. This transformation in the shape of surface intrusions, from sharp notches to more rounded forms, was a direct result of the HIP process. The influence of the HIP process on the surface roughness of the samples was observed in the µ-CT data obtained from the vertical cross-sections, as depicted in Figure 6B. The HIPed samples exhibited less variation in height and higher curvature in the valleys compared to the as-built samples, clearly demonstrating this effect.

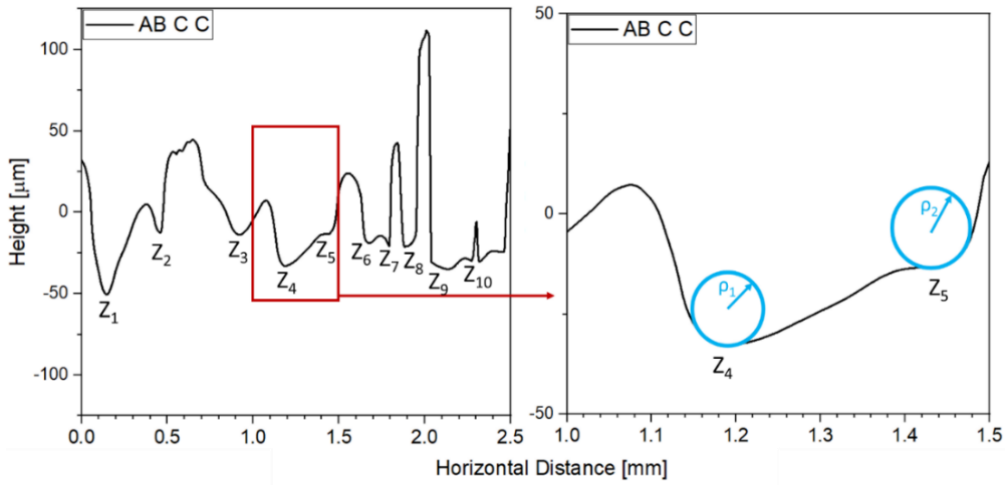

Figure 12. (left) A line scan taken from the surface of an as-built L-PBF sample fabricated with coarse powder and contouring (sample AB-C-C) and (right) two examples showing the measurements of the radii of the deepest valleys.

Table 5. Surface roughness metrics and stress concentration factors computed using Eq. 3-9 for Ti-6Al-4V samples processed via L-PBF, with variations in conditions.

Sample	R_a [µm]	R_t [µm]	R_{zISO} [µm]	$\bar{\rho}_{10}$ [µm]	q	$\overline{K_t}$	$\overline{K_f}$
AB-C-C	29.68 ± 4.5	162.28 ± 23.2	162.28 ± 23.1	24.77 ± 7.6	0.95	3.39	3.27
AB-C-NC	29.05 ± 5.6	197.09 ± 21.6	197.09 ± 21.5	22.56 ± 5.5	0.94	3.57	3.43
AB-F-C	20.44 ± 3.4	118.36 ± 25.1	118.36 ± 25.2	27.66 ± 6.5	0.95	2.47	2.41
AB-F-NC	22.98 ± 5.3	163.89 ± 22.3	163.89 ± 22.3	19.71 ± 7.2	0.93	3.33	3.18
HIP-C-C	21.30 ± 4.7	109.13 ± 26.2	109.13 ± 26.1	24 ± 8.1	0.93	2.77	2.65
HIP-C-NC	25.93 ± 4.3	144.24 ± 25.4	144.24 ± 25.5	30.66 ± 6.2	0.94	2.69	2.60
HIP-F-C	17.94 ± 3.2	112.98 ± 21.7	112.98 ± 21.7	25.57 ± 5.4	0.93	2.40	2.31
HIP-F-NC	23.03 ± 4.1	159.24 ± 24.6	159.24 ± 24.6	21.42 ± 6.8	0.92	3.14	2.99

4.11. Fatigue modeling based on surface roughness

The fatigue endurance calculated using Eq. 2 can be used to create a model to estimate the fatigue performance of the samples. As stated in the work by Budynas and Nisbett [72], the fatigue strength of the samples are directly correlated with their ultimate tensile strength (UTS), as follows:

$$\sigma'_3 = f\sigma_{UT} \tag{10}$$

where f is the fatigue strength fraction factor and σ_{UT} is the UTS. The average reported UTS value of the L-PBF processed Ti-6Al-4V is 1074±70 MPa [18,73–76] and 940±29 MPa [19,77,78] in the as-built and HIP conditions, respectively. The f value was taken from Ref. [72] is 0.79 for the Ti-6Al-4V alloy. By considering the different experimental fatigue endurances for the samples in different conditions in this study, and the calculated σ'_3 value for the samples, a linear line can be drawn on the log-log fatigue graphs [33] as shown in Figure 13A. By using this line, the fatigue performance of the samples under any stress can be estimated. Here, the same stress amplitudes as the fatigue experiments were fed to the models and the output of the models were plotted against the experimental cycles to failure values (see Figure 13B). The data points in these figures are within the scatter band of 2 which shows the reasonable accuracy of using these calculations for predicting the fatigue life of the L-PBF processed non-spherical Ti-6Al-4V powders under various conditions. Moreover, these calculations can be considered a valuable design tool when a certain set of data for a specific condition is not available.

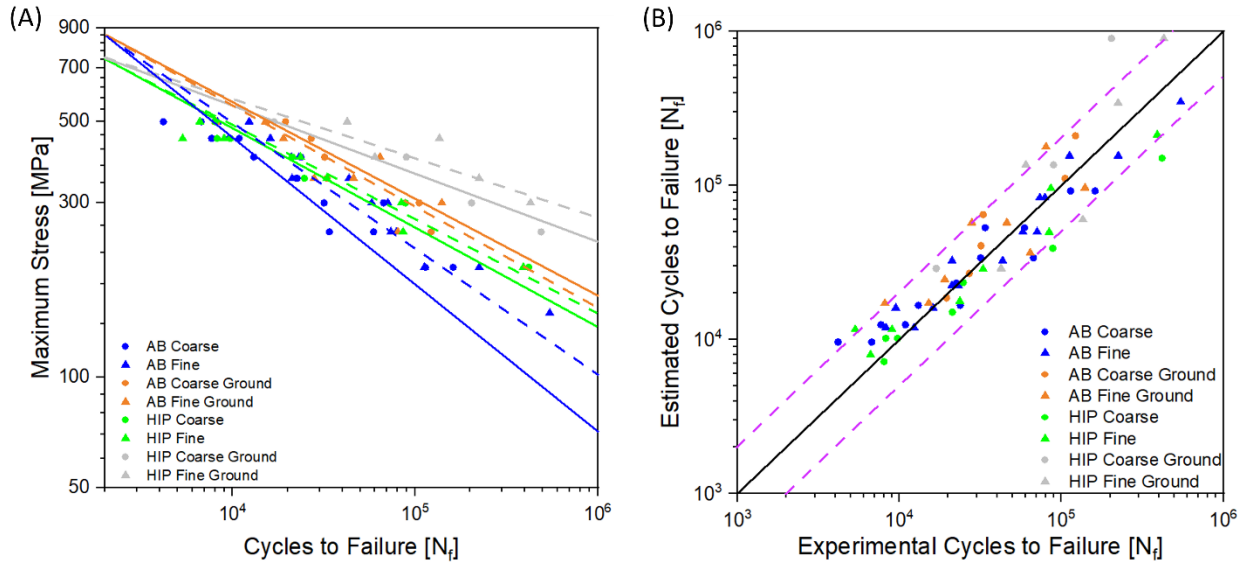

Figure 13. (A) Curves plotted for fatigue prediction derived from the Arola-Ramulu model and (B) the calculated fatigue performance compared to experimental data with the scatter band of 2. Note that the estimated cycles to failure in (B) were calculated using the linear equations obtained from (A).

The same approach was taken by previous studies [33,71] in an attempt to create a model for predicting the fatigue life of the L-PBF processed Ti-6Al-4V parts using spherical powder,

however, their calculations only considered a specific condition of surface treatment to study the effect of surface treatment on the fatigue life. In the current study, the calculations were performed to re-create the Arola-Ramulu [69] model for the samples subjected to various post-treatments such as HIP, and mechanical grinding processes. It is worth noting that the mentioned studies also used the EOS M290 machine to manufacture their samples which is the same machine used in the current study, therefore, the new insights from this study are reasonably comparable to that of the published literature.

4.12. Fracture mechanisms

In our current study, the HIP samples followed a facet formation mechanism due to dislocation pile-ups, while the as-built samples exhibited a pseudo-brittle fracture mechanism resulting from a localized deformations, as reported in our previous study in [15] and shown in Figure 14A and 14B. The schematic representation of theses distinct fracture mechanisms in Ti-6Al-4V samples with different microstructures is illustrated in Figure 14C.

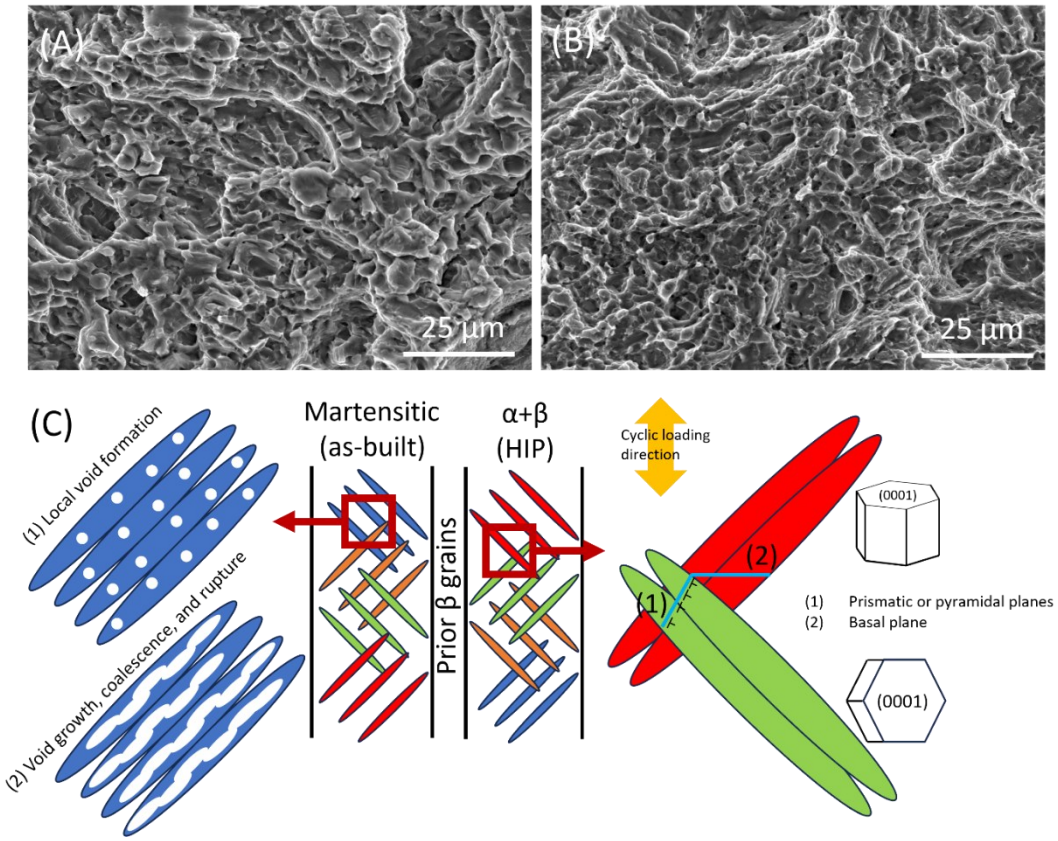

Figure 14. Micrographs of the fracture surfaces of the L-PBF processed Ti-6Al-4V non-spherical fine powder tested under 500 MPa in (A) as-built and (B) HIPed conditions. (C) Schematic showing the fracture proposed mechanisms in the martensitic microstructure in the as-built sample (on the left) and α+β microstructure in the HIP samples (on the right). For direct presentation of lath size and organization of the laths, refer to Figure 2.

Crack initiation in fusion-based AM Ti-6Al-4V, mainly in the samples exhibiting an α+β microstructure, has been extensively reported and is associated with the formation of facets within the α phase [62,79]. One explanation for the formation of these facets at interfaces within the α phase is based on having few available slip planes and the inherent anisotropy of the hexagonal closed-packed (HCP) lattice, as previously noted by Neal *et al*. [80] and Dunne *et al*. [81].

Bache's widely recognized theory [82] proposes that the orientation of adjacent grains influences slip behavior: the first grain aligns prismatic or pyramidal planes with the load axis to facilitate slip, while the second grain's basal plane is oriented perpendicular to the load axis to inhibit slip. This arrangement causes dislocations to accumulate at the grain boundary between the two grains. Shear and tensile stresses on the basal plane of the second grain lead to the formation of facets, which concentrate stress at the grain boundary and induce a ductile fracture in the first grain. This fracture then propagates through the grain boundary into the second grain.

Everaets et al. [83] offer an alternative theory where the second grain is also oriented favorably for slip but with a slight misorientation that creates grain boundaries. In this scenario, facets develop within the first grain, and the crack moves into the second grain with minimal resistance at the boundary. This type of facet formation is more pronounced in materials with an equiaxed α phase compared to those with a basket-weave α+β microstructure.

In contrast, the fracture behavior in martensitic Ti-6Al-4V parts differs significantly. Moridi et al. [84] found that in L-PBF processed Ti-6Al-4V with a martensitic microstructure, fracture results from localized deformation within α′ laths. Voids form within primary α′ laths oriented at 45° to the load axis, where they experience a high Schmid factor. These voids expand under loading, eventually linking within the α′ laths and causing a ductile final fracture. However, fractures between the α′ laths are brittle. Thus, while the fracture mechanism is ductile microscopically, it appears more brittle macroscopically.

4. Conclusion

This research investigated the influence of various factors including powder characteristics (non-spherical morphology and particle size ranging from 50-120 μm or 75-175 μm), process conditions during L-PBF (contouring), and post-processing treatments (HIP and mechanical grinding) on the pore levels, microstructural features, surface quality, and fatigue performance of additively manufactured Ti-6Al-4V specimens. The following conclusions are made:

- The fatigue performance of components made from non-spherical powders was found to be similar to those made from spherical powders, irrespective of the powder size. Fine non-spherical powders exhibited a marginally better fatigue life than coarse powders.
- Mechanical surface grinding was effective in improving fatigue performance. However, sub-surface pores still limited overall fatigue performance, regardless of whether they were

exposed on the surface (Figure 7A). Additionally, contouring did not significantly alter fatigue performance, despite a slight reduction in surface roughness (Figure 7B).

- The HIP process effectively sealed internal pores but did not impact sub-surface pores that were connected to the surface. This process also transformed the component's microstructure from α′ martensitic to α+β, enhancing ductility and shifting the fracture mechanism from pseudo-brittle to facet formation.
- Combining HIP treatment with mechanical grinding was the most effective post-processing method for improving fatigue performance. This combination nearly eliminated all surface, sub-surface, and internal pores and transformed the brittle α′ phase, resulting in fatigue performance close to that of wrought materials.
- Correlation analysis using Pearson, Spearman, and Kendall Tau methods indicated strong negative correlations between R_v and contour, as well as between pore count and HIP treatment. Positive correlations were observed between the fatigue strength exponent "*b*" and contouring. ANOVA results confirmed these correlations, showing significant differences in Rv and pore count across groups. Tukey's HSD Test further identified specific group differences.
- Fatigue lives were analyzed in relation to surface roughness. Fatigue modeling, using the linear relationship between σ'_3 and endurance based on the Arola-Ramulu model, accurately predicted fatigue lives for L-PBF Ti-6Al-4V samples with various surface roughness levels, with most data falling within the acceptable scatter band of 2.

Acknowledgements

AM acknowledges the startup funding provided by the Mechanical, Materials, and Aerospace Engineering Department at the Illinois Institute of Technology in Chicago, Illinois. The authors acknowledge support from the National Science Foundation under grant number DMR-2050916 and CMMI-2339857. Additionally, this research received support from the Pennsylvania Infrastructure Technology Alliance, which is a collaboration between Carnegie Mellon University, Lehigh University, and the Department of Community and Economic Development (DCED) of the Commonwealth of Pennsylvania. The authors extend their gratitude to Reading Alloys (now part of Kymera International) and Mike Marucci for supplying the Ti-6Al-4V powder used in this study and for their valuable assistance. ADR acknowledges support from a NASA University Leadership Initiative under Grant number 80NSSC19M0123. Special thanks are also given to Dr. Ziheng Wu for his assistance with the part production process at CMU.

References

[1] J. Qian, D. Dong, G. Wei, M. Shi, S. Tang, A method for the preparation of spherical titanium powder for additive manufacturing, Powder Technol. 411 (2022) 117927.

[2] G. Chen, S.Y. Zhao, P. Tan, J. Wang, C.S. Xiang, H.P. Tang, A comparative study of Ti-6Al-4V powders for additive manufacturing by gas atomization, plasma rotating electrode process and plasma atomization, Powder Technol. 333 (2018) 38–46.

[3] R. Cunningham, A. Nicolas, J. Madsen, E. Fodran, E. Anagnostou, M.D. Sangid, A.D. Rollett, Analyzing the effects of powder and post-processing on porosity and properties of electron beam melted Ti-6Al-4V, Mater. Res. Lett. 5 (2017) 516–525.

[4] J. Guzmán, R. de M. Nobre, E.R. Nunes, D.L. Bayerlein, R.B. Falcão, E. Sallica-Leva, J.B.F. Neto, H.R. Oliveira, V.L. Chastinet, F.J.G. Landgraf, Laser powder bed fusion parameters to produce high-density Ti–53%Nb alloy using irregularly shaped powder from hydride-dehydride (HDH) process, J. Mater. Res. Technol. 10 (2021) 1372–1381.

[5] F. Mendina, Reducing Metal Alloy Powder Costs For Use In Powder Bed Fusion Additive Manufacturing: Improving The Economics For Production, ProQuest Diss. Theses Glob. (2013) 13–18.

[6] Conversation of Dr. Brandon McWilliams, Chief (A) Manufacturing Sci. and Tech. Branch, (n.d.).

[7] J.H. Martin, J.E. Barnes, K.A. Rogers, J. Hundley, D.L. Laplant, S. Ghanbari, J. Tsai, D.F. Bahr, Additive manufacturing of a high-performance aluminum alloy from cold mechanically derived non-spherical powder, Nat. Commun. Mater. 4 (2023) 39.

[8] M. Asherloo, Z. Wu, E. Ghebreiesus, S. Fryzlewicz, R. Jiang, B. Gould, M. Heim, D. Nelson, M. Marucci, M. Paliwal, A.D. Rollett, A. Mostafaei, Laser-beam powder bed fusion of cost-effective non-spherical hydride-dehydride Ti-6Al-4V alloy, Addit. Manuf. 56 (2022) 102875.

[9] Z. Wu, M. Asherloo, R. Jiang, M.H. Delpazir, N. Sivakumar, M. Paliwal, J. Capone, B. Gould, A. Rollett, A. Mostafaei, Study of Printability and Porosity Formation in Laser Powder Bed Fusion Built Hydride-Dehydride (HDH) Ti-6Al-4V, Addit. Manuf. 47 (2021) 102323.

[10] S.P. Narra, Z. Wu, R. Patel, J. Capone, M. Paliwal, J. Beuth, A.D. Rollett, Use of Non-Spherical Hydride-DeHydride (HDH) Powders in Powder Bed Fusion Additive Manufacturing, Addit. Manuf. 34 (2020) 101188.

[11] X. Yang, Z. Zhang, W. Gu, B. Wang, Y. Fan, Q. Miao, S. Zhao, B. Xie, Fabrication of ultra-low-cost pure Ti by selective laser melting using the mixed powders of hydride-dehydride titanium powders treated by ball milling and spherical powders, Powder Metall. 64 (2021) 35–42.

[12] P. Edwards, M. Ramulu, Fatigue performance evaluation of selective laser melted Ti-6Al-4V, Mater. Sci. Eng. A. 598 (2014) 327–337.

[13] Y. Yang, M. Zhao, H. Wang, K. Zhou, Y. He, Y. Mao, D. Xie, F. Lv, L. Shen, Microstructure and Fatigue Performance of Ti6Al4V Produced by Laser Powder Bed Fusion after Post-Heat Treatment, Appl. Sci. 13 (2023).

[14] S. Moon, R. Ma, R. Attardo, C. Tomonto, M. Nordin, P. Wheelock, M. Glavicic, M. Layman, R. Billo, T. Luo, Impact of surface and pore characteristics on fatigue life of

laser powder bed fusion Ti–6Al–4V alloy described by neural network models, Sci. Rep. 11 (2021) 20424.
[15] M. Asherloo, Z. Wu, M. Heim, D. Nelson, M. Paliwal, A.D. Rollett, A. Mostafaei, Fatigue performance of laser powder bed fusion hydride-dehydride Ti-6Al-4V powder, Addit. Manuf. 59 (2022) 103117.
[16] M. Benedetti, M. Cazzolli, V. Fontanari, M. Leoni, Fatigue limit of Ti6Al4V alloy produced by Selective Laser Sintering, Procedia Struct. Integr. 2 (2016) 3158–3167.
[17] M. Roudnicka, K. Mertova, D. Vojtech, Influence of hot isostatic pressing on mechanical response of as-built SLM titanium alloy, IOP Conf. Ser. Mater. Sci. Eng. 629 (2019) 12034.
[18] S. Leuders, M. Thöne, A. Riemer, T. Niendorf, T. Tröster, H.A. Richard, H.J. Maier, On the mechanical behaviour of titanium alloy TiAl6V4 manufactured by selective laser melting: Fatigue resistance and crack growth performance, Int. J. Fatigue. 48 (2013) 300–307.
[19] G. Kasperovich, J. Hausmann, Improvement of fatigue resistance and ductility of TiAl6V4 processed by selective laser melting, J. Mater. Process. Technol. 220 (2015) 202–214.
[20] J.M. Alegre, A. Díaz, R. García, L.B. Peral, I.I. Cuesta, Effect of HIP post-processing at 850 °C/200 MPa in the fatigue behavior of Ti-6Al-4V alloy fabricated by Selective Laser Melting, Int. J. Fatigue. 163 (2022) 107097.
[21] ASTM B348: Standard Specification for Titanium and Titanium Alloy Bars and Billets, Vol 02.04, (n.d.).
[22] M. Asherloo, Z. Wu, J.E.C. Sabisch, I. Ghamarian, A.D. Rollett, A. Mostafaei, Variant selection in laser powder bed fusion of non-spherical Ti-6Al-4V powder, J. Mater. Sci. Technol. 147 (2023) 56–67.
[23] M. Asherloo, J. Hwang, R. Leroux, Z. Wu, K. Fezzaa, M. Paliwal, A.D. Rollett, A. Mostafaei, Understanding process-microstructure-property relationships in laser powder bed fusion of non-spherical Ti-6Al-4V powder, Mater. Charact. 198 (2023) 112757.
[24] S.A. Etesami, B. Fotovvati, E. Asadi, Heat treatment of Ti-6Al-4V alloy manufactured by laser-based powder-bed fusion: Process, microstructures, and mechanical properties correlations, J. Alloys Compd. 895 (2022) 162618.
[25] F. Bachmann, R. Hielscher, H. Schaeben, Texture Analysis with MTEX – Free and Open Source Software Toolbox, Solid State Phenom. 160 (2010) 63–68.
[26] S. Gates-Rector, T. Blanton, The Powder Diffraction File: a quality materials characterization database, Powder Diffr. 34 (2019) 1–9.
[27] L. Lutterotti, Total pattern fitting for the combined size–strain–stress–texture determination in thin film diffraction, Nucl. Instruments Methods Phys. Res. Sect. B Beam Interact. with Mater. Atoms. 268 (2010) 334–340.
[28] K. Esmati, A. Chakraborty, S. Pendurti, A. Natarajan, É. Martin, Anisotropic sintering behavior of stainless steel 316L printed by binder jetting additive manufacturing, Mater. Today Commun. (2024) 110528.
[29] A. Shaikh, S. Kirwai, A. Patil, A. Shaikh, S. Kumar, Effect of Temperature and Cooling Rates on the α + β Morphology of Effect of Temperature and Cooling Rates on the α + β Morphology of Ti-6Al-4V Alloy Ti-6Al-4V Alloy, Procedia Struct. Integr. 14 (2019)

782–789.
[30] Melody H. Delpazir, M. Asherloo, S.N.K. Abad, A. Thompson, V. Guma, S.D. Bagi, K.K. Sreenivas, M. Paliwal, J. Terry, A.D. Rollett, A. Mostafaei, Microstructure and corrosion behavior of differently heat-treated Ti-6Al-4V alloy processed by laser powder bed fusion of hydride-dehydride powder, Corros. Sci. (2023) 111495.
[31] R.J. Morrissey, T. Nicholas, Fatigue strength of Ti–6Al–4V at very long lives, Int. J. Fatigue. 27 (2005) 1608–1612.
[32] M. Peters, J. Hemptenmacher, J. Kumpfert, C. Leyens, Structure and Properties of Titanium and Titanium Alloys, 2005.
[33] S. Lee, B. Rasoolian, D.F. Silva, J.W. Pegues, N. Shamsaei, Surface roughness parameter and modeling for fatigue behavior of additive manufactured parts: A non-destructive data-driven approach, Addit. Manuf. 46 (2021) 102094.
[34] A. Soltani-Tehrani, M. Habibnejad-Korayem, S. Shao, M. Haghshenas, N. Shamsaei, Ti-6Al-4V powder characteristics in laser powder bed fusion: The effect on tensile and fatigue behavior, Addit. Manuf. 51 (2022) 102584.
[35] J. Pegues, M. Roach, R. Scott Williamson, N. Shamsaei, Surface roughness effects on the fatigue strength of additively manufactured Ti-6Al-4V, Int. J. Fatigue. 116 (2018) 543–552.
[36] S. Dai, Y. Zhu, Z. Huang, Microstructure evolution and strengthening mechanisms of pure titanium with nano-structured surface obtained by high energy shot peening, Vacuum. 125 (2016) 215–221.
[37] C.A. Kantzos, R.W. Cunningham, V. Tari, A.D. Rollett, Characterization of metal additive manufacturing surfaces using synchrotron X-ray CT and micromechanical modeling, Comput. Mech. 61 (2018) 575–580.
[38] A. Mostafaei, C. Zhao, Y. He, S. Reza Ghiaasiaan, B. Shi, S. Shao, N. Shamsaei, Z. Wu, N. Kouraytem, T. Sun, J. Pauza, J. V. Gordon, B. Webler, N.D. Parab, M. Asherloo, Q. Guo, L. Chen, A.D. Rollett, Defects and anomalies in powder bed fusion metal additive manufacturing, Curr. Opin. Solid State Mater. Sci. 26 (2022) 100974.
[39] C.-W. Lin, C.-P. Ju, J.-H. Chern Lin, A comparison of the fatigue behavior of cast Ti–7.5Mo with c.p. titanium, Ti–6Al–4V and Ti–13Nb–13Zr alloys, Biomaterials. 26 (2005) 2899–2907.
[40] N. Sanaei, A. Fatemi, Analysis of the effect of internal defects on fatigue performance of additive manufactured metals, Mater. Sci. Eng. A. 785 (2020) 139385.
[41] F.C. Campbell, Fatigue and fracture: understanding the basics, ASM International, 2012.
[42] M. Gharbi, P. Peyre, C. Gorny, M. Carin, S. Morville, P. Le Masson, D. Carron, R. Fabbro, Influence of various process conditions on surface finishes induced by the direct metal deposition laser technique on a Ti-6Al-4V alloy, J. Mater. Process. Technol. 213 (2013) 791–800.
[43] S. Lou, X. Jiang, W. Sun, W. Zeng, L. Pagani, P.J. Scott, Characterisation methods for powder bed fusion processed surface topography, Precis. Eng. 57 (2019) 1–15.
[44] J. Gockel, L. Sheridan, B. Koerper, B. Whip, The influence of additive manufacturing processing parameters on surface roughness and fatigue life, Int. J. Fatigue. 124 (2019) 380–388.
[45] A. Triantaphyllou, C.L. Giusca, G.D. Macaulay, F. Roerig, M. Hoebel, R.K. Leach, B.

Tomita, K.A. Milne, Surface texture measurement for additive manufacturing, Surf. Topogr. Metrol. Prop. 3 (2015).
[46] J. Karlsson, A. Snis, H. Engqvist, J. Lausmaa, Characterization and comparison of materials produced by Electron Beam Melting (EBM) of two different Ti-6Al-4V powder fractions, J. Mater. Process. Technol. 213 (2013) 2109–2118.
[47] S. Sendino, S. Martinez, F. Lartategui, M. Gardon, A. Lamikiz, J.J. Gonzalez, Effect of powder particle size distribution on the surface finish of components manufactured by laser powder bed fusion, Int. J. Adv. Manuf. Technol. 124 (2023) 789–799.
[48] A.B. Spierings, N. Herres, G. Levy, Influence of the particle size distribution on surface quality and mechanical properties in AM steel parts, Rapid Prototyp. J. 17 (2011) 195–202.
[49] B. Vayssette, N. Saintier, C. Brugger, M. El May, E. Pessard, Numerical modelling of surface roughness effect on the fatigue behavior of Ti-6Al-4V obtained by additive manufacturing, Int. J. Fatigue. 123 (2019) 180–195.
[50] J.C. Fox, S.P. Moylan, B.M. Lane, Effect of Process Parameters on the Surface Roughness of Overhanging Structures in Laser Powder Bed Fusion Additive Manufacturing, Procedia CIRP. 45 (2016) 131–134.
[51] P. Karimi, C. Schnur, E. Sadeghi, J. Andersson, Contour design to improve topographical and microstructuralcharacteristics of Alloy 718 manufactured using electron beam-powderbed fusion, Addit. Manuf. (2019).
[52] M.A. Groeber, E. Schwalbach, S. Donegan, K. Chaput, T. Butler, J. Miller, Application of characterization, modelling, and analytics towards understanding process-structure linkages in metallic 3D printing, IOP Conf. Ser. Mater. Sci. Eng. 219 (2017).
[53] Khairallah, S.A., Anderson, A.T.,Rubenchik, A., King, W.E., Laser powder-bed fusion additive manufacturing: Physics of complex melt flow and formation mechanisms of pores, spatter, and denudation zones Saad, Acta Mater. 108 (n.d.) 36–45.
[54] A.A. Martin, N.P. Calta, S.A. Khairallah, J. Wang, P.J. Depond, A.Y. Fong, V. Thampy, G.M. Guss, A.M. Kiss, K.H. Stone, C.J. Tassone, J.N. Weker, M.F. Toney, T. Van Buuren, M.J. Matthews, Dynamics of pore formation during laser powder bed fusion additive manufacturing bed fusion additive manufacturing, Nat. Commun. 10 (2019) 1–10.
[55] L. Thijs, K. Kempen, J.P. Kruth, J. Van Humbeeck, Fine-structured aluminium products with controllable texture by selective laser melting of pre-alloyed AlSi10Mg powder, Acta Mater. 61 (2013) 1809–1819.
[56] C. Zhao, N.D. Parab, X. Li, K. Fezzaa, W. Tan, A.D. Rollett, T. Sun, Critical instability at moving keyhole tip generates porosity in laser melting, Science (80-.). 1086 (2020) 1080–1086.
[57] T. Mishurova, K. Artzt, J. Haubrich, G. Requena, G. Bruno, Exploring the correlation between subsurface residual stresses and manufacturing parameters in laser powder bed fused ti-6al-4v, Metals (Basel). 9 (2019).
[58] H. Karimialavijeh, M. Ghasri-Khouzani, A. Das, M. Pröebstle, É. Martin, Effect of laser contour scan parameters on fatigue performance of A20X fabricated by laser powder bed fusion, Int. J. Fatigue. 175 (2023) 107775.
[59] M. Bonesso, P. Rebesan, C. Gennari, S. Mancin, R. Dima, A. Pepato, I. Calliari, Effect of

Particle Size Distribution on Laser Powder Bed Fusion Manufacturability of Copper, BHM Berg- Und Hüttenmännische Monatshefte. 166 (2021) 256–262.
[60] T. Kosonen, K. Kakko, N. Raitanen, Evaluation of pore re-opening after HIP in LPBF Ti–6Al–4V, Powder Metall. 64 (2021) 425–433.
[61] N. Sanaei, A. Fatemi, N. Phan, Defect characteristics and analysis of their variability in metal L-PBF additive manufacturing, Mater. Des. 182 (2019) 108091.
[62] J. Günther, D. Krewerth, T. Lippmann, S. Leuders, T. Tröster, A. Weidner, H. Biermann, T. Niendorf, Fatigue life of additively manufactured Ti–6Al–4V in the very high cycle fatigue regime, Int. J. Fatigue. 94 (2017) 236–245.
[63] N. Sanaei, A. Fatemi, Defects in Additive Manufactured Metals and Their Effect on Fatigue Performance: A State-of-the-Art Review, Prog. Mater. Sci. (2020) 100724.
[64] A. Mostafaei, S.H.V.R. Neelapu, C. Kisailus, L.M. Nath, T.D.B. Jacobs, M. Chmielus, Characterizing surface finish and fatigue behavior in binder-jet 3D-printed nickel-based superalloy 625, Addit. Manuf. 24 (2018) 200–209.
[65] Y. Murakami, M. Endo, Effects of defects, inclusions and inhomogeneities on fatigue strength, Int. J. Fatigue. 16 (1994) 163–182.
[66] M. Benedetti, V. Fontanari, M. Bandini, F. Zanini, S. Carmignato, Low- and high-cycle fatigue resistance of Ti-6Al-4V ELI additively manufactured via selective laser melting: Mean stress and defect sensitivity, Int. J. Fatigue. 107 (2018) 96–109.
[67] H. Masuo, Y. Tanaka, S. Morokoshi, H. Yagura, T. Uchida, Y.Y. Yamamoto, Y. Murakami, Influence of defects, surface roughness and HIP on the fatigue strength of Ti-6Al-4V manufactured by additive manufacturing, Int. J. Fatigue. 117 (2018) 163–179.
[68] H. Neuber, Theory of notch stresses: principles for exact calculation of strength with reference to structural form and material, USAEC Office of Technical Information, 1961.
[69] D. Arola, M. Ramulu, An examination of the effects from surface texture on the strength of fiber reinforced plastics, J. Compos. Mater. 33 (1999) 102–123.
[70] ASTM B946-06 Standard Test Method for Surface Finish of Powder Metallurgy (P/M) Products, (2006).
[71] J.W. Pegues, N. Shamsaei, M.D. Roach, R.S. Williamson, Fatigue life estimation of additive manufactured parts in the as-built surface condition, Mater. Des. Process. Commun. 1 (2019) e36.
[72] R.G. Budynas, J.K. Nisbett, Mechanical Engineern Design, 2007.
[73] T. Vilaro, C. Colin, J.D. Bartout, As-fabricated and heat-treated microstructures of the Ti-6Al-4V alloy processed by selective laser melting, Metall. Mater. Trans. A Phys. Metall. Mater. Sci. 42 (2011) 3190–3199.
[74] S. Cao, R. Chu, X. Zhou, K. Yang, Q. Jia, C.V.S. Lim, A. Huang, X. Wu, Role of martensite decomposition in tensile properties of selective laser melted Ti-6Al-4V, J. Alloys Compd. 744 (2018) 357–363.
[75] X. Shi, C. Yan, W. Feng, Y. Zhang, Z. Leng, Effect of high layer thickness on surface quality and defect behavior of Ti-6Al-4V fabricated by selective laser melting, Opt. Laser Technol. 132 (2020) 106471.
[76] Y. Yang, Y.J. liu, J. Chen, H.L. Wang, Z.Q. Zhang, Y.J. Lu, S.Q. Wu, J.X. Lin, Crystallographic features of α variants and β phase for Ti-6Al-4V alloy fabricated by selective laser melting, Mater. Sci. Eng. A. 707 (2017) 548–558.

[77] S. Leuders, T. Lieneke, S. Lammers, T. Tröster, T. Niendorf, On the fatigue properties of metals manufactured by selective laser melting – The role of ductility, J. Mater. Res. 29 (2014) 1911–1919.
[78] M. Benedetti, E. Torresani, M. Leoni, V. Fontanari, M. Bandini, C. Pederzolli, C. Potrich, The effect of post-sintering treatments on the fatigue and biological behavior of Ti-6Al-4V ELI parts made by selective laser melting, J. Mech. Behav. Biomed. Mater. 71 (2017) 295–306.
[79] Y. Zhai, H. Galarraga, D.A. Lados, Microstructure, static properties, and fatigue crack growth mechanisms in Ti-6Al-4V fabricated by additive manufacturing: LENS and EBM, Eng. Fail. Anal. 69 (2016) 3–14.
[80] D.F. Neal, P.A. Blenkinsop, Internal fatigue origins in α-β titanium allols, Acta Metall. 24 (1976) 59–63.
[81] F.P.E. DUNNE, D. RUGG, On the mechanisms of fatigue facet nucleation in titanium alloys, Fatigue Fract. Eng. Mater. Struct. 31 (2008) 949–958.
[82] M.R. Bache, Processing titanium alloys for optimum fatigue performance, Int. J. Fatigue. 21 (1999) S105–S111.
[83] J. Everaerts, B. Verlinden, M. Wevers, The influence of the alpha grain size on internal fatigue crack initiation in drawn Ti-6Al-4V wires, Procedia Struct. Integr. 2 (2016) 1055–1062.
[84] A. Moridi, A.G. Demir, L. Caprio, A.J. Hart, B. Previtali, B.M. Colosimo, Deformation and failure mechanisms of Ti–6Al–4V as built by selective laser melting, Mater. Sci. Eng. A. 768 (2019) 1–25.